# Scaling studies of QCD with the dynamical HISQ action

A. Bazavov, W. Freeman, and D. Toussaint

*Department of Physics, University of Arizona, Tucson, AZ 85721, USA*

C. Bernard and J. Laiho *

*Department of Physics, Washington University, St. Louis, MO 63130, USA*

C. DeTar, L. Levkova, and M. Oktay

*Physics Department, University of Utah, Salt Lake City, UT 84112, USA*

Steven Gottlieb

*Department of Physics, Indiana University, Bloomington, IN 47405, USA and*

*National Center for Supercomputing Applications,*

*University of Illinois, Urbana, IL 61801, USA*

U.M. Heller

*American Physical Society, One Research Road, Ridge, NY 11961, USA*

J.E. Hetrick

*Physics Department, University of the Pacific, Stockton, CA 95211, USA*

J. Osborn

*Argonne Leadership Computing Facility,*

*Argonne National Laboratory, Argonne, IL 60439, USA*

R.L. Sugar

*Department of Physics, University of California, Santa Barbara, CA 93106, USA*

R.S. Van de Water

*Department of Physics, Brookhaven National Laboratory, Upton, NY 11973, USA*

[MILC Collaboration]

---

* Present address: University of Glasgow, Glasgow G12 8QQ, UK

## Abstract

We study the lattice spacing dependence, or scaling, of physical quantities using the highly improved staggered quark (HISQ) action introduced by the HPQCD/UKQCD collaboration, comparing our results to similar simulations with the asqtad fermion action. Results are based on calculations with lattice spacings approximately 0.15, 0.12 and 0.09 fm, using four flavors of dynamical HISQ quarks. The strange and charm quark masses are near their physical values, and the light-quark mass is set to 0.2 times the strange-quark mass. We look at the lattice spacing dependence of hadron masses, pseudoscalar meson decay constants, and the topological susceptibility. In addition to the commonly used determination of the lattice spacing through the static quark potential, we examine a determination proposed by the HPQCD collaboration that uses the decay constant of a fictitious "unmixed $s\bar{s}$" pseudoscalar meson. We find that the lattice artifacts in the HISQ simulations are much smaller than those in the asqtad simulations at the same lattice spacings and quark masses.

# I. INTRODUCTION AND MOTIVATION

The "highly improved staggered quark", or HISQ, action was developed by the HPQCD/UKQCD collaboration to reduce the lattice artifacts associated with staggered quarks in lattice QCD calculations [1–3]. While significantly more expensive than the asqtad action used in the MILC collaboration's long-running program of QCD simulations with three dynamical quark flavors [4], it is still very economical compared with non-staggered quark actions.

The initial studies of the HISQ action by the HPQCD/UKQCD collaboration demonstrated the reduction of taste symmetry breaking and improvements in the dispersion relation for the charm quark by using the HISQ action for valence quarks on quenched lattices and lattices generated with asqtad sea quarks [1–3]. Further work with this action, again implemented for the valence quarks with asqtad sea quarks, has demonstrated impressive precision for charmonium and heavy-light meson physics [5–7].

As a first stage in a complete program of QCD simulations using the HISQ action for dynamical quarks, we have generated ensembles of lattices at three different lattice spacings with four flavors of dynamical quarks, where the light-quark mass is fixed at two-tenths of the strange quark mass, and the strange and charm quark masses are near their physical values. This allows us to test scaling, or dependence of calculated quantities on the lattice spacing. The purpose of this paper is to report on these tests at fixed quark mass. Where possible, we compare the lattice spacing dependence of physical quantities with the HISQ action to their dependence using the asqtad action at the same quark mass and lattice spacings. We look at the static quark potential, splittings among the different tastes of pions, masses of the rho and nucleon, pseudoscalar meson decay constants and the topological susceptibility. We emphasize that all of this is done at a fixed, and unphysically large, light-quark mass — our purpose here is to make a controlled study of the dependence on lattice spacing.

# II. METHODS AND LATTICE DATA

There are four major differences between these HISQ simulations and our earlier asqtad simulations.

First, the HISQ simulations include the effects of a dynamical charm quark. We expect

that the effects of dynamical charm will be very small for the quantities studied here, but with modern algorithms it is cheap to include the charm quark, and we plan to investigate quantities involving dynamical charm in the future.

Second, the one-quark-loop contributions to the perturbative calculation of the coefficients in the Symanzik improved gauge action are included. At the time the asqtad simulation program was started these corrections were not available, but they have now been computed for both the asqtad and HISQ actions, and are unexpectedly large [8].

Third, in the HISQ action the parallel transport of quark fields is done with a link that is highly smeared. Specifically, it is first smeared using a "fat7" smearing, then projected onto a unitary matrix, and then smeared again with an "asqtad" smearing [3]. The use of the asqtad smearing in the second iteration, together with the addition of the Naik term, or third-nearest-neighbor coupling, in $\slashed{D}$, insures that the fermion action is formally order $a^2$ improved. The use of two levels of smearing produces a smooth gauge field as seen by the quarks, and this explains the reduced taste symmetry violations.

Finally, the third-nearest-neighbor term in the charm quark $\slashed{D}$ is modified to improve the charm quark dispersion relation [3]. These last two differences combine to make up what is usually meant by "the HISQ action", although in principle they could be introduced independently.

Where practical, since our purpose is to compare the lattice artifacts in the two actions, we use the same analysis for the HISQ data as was used for the asqtad data.

Table I shows the parameters of the three HISQ runs used in these tests. Detailed information about the asqtad ensembles can be found in Ref. [4].

The HISQ lattices were generated using the rational hybrid Monte Carlo (RHMC) algorithm [9]. Issues with implementing this algorithm for the HISQ action have been discussed in Ref. [10]. We used different molecular dynamics step sizes for the gauge and fermion parts of the action, with three gauge steps for each fermion step [11]. We used the Omelyan integration algorithm in both the gauge and fermion parts [11, 12]. Five pseudofermion fields were used, each with a rational function approximation for the fractional powers. The first implements the ratio of the roots of the determinants for the light and strange sea quarks to the determinant for three heavy "regulator" quarks with mass $am_r = 0.2$. That is, it corresponds to the weight $\det{(M(m_l))}^{1/2} \det{(M(m_s))}^{1/4} \det{(M(m_r))}^{-3/4}$. The next three pseudofermion fields each implement the force from one flavor of the regulator quark, or the

TABLE I: Parameters of the HISQ runs with $m_l = 0.2\,m_s$. Here $\epsilon_N$ is the correction for the three link (Naik) term in the charm quark action. These values differ slightly from the expression in Appendix A because they do not include the distinction between bare and tree-level quark mass (see Eq. (24) in Ref. [3].) The expression in Appendix A is used in all more recent ensembles. The number of equilibrated lattices is $N_{lats}$. The separation of the lattices in simulation time is $S_t$, the length of a trajectory in simulation time is $L_t$, the molecular dynamics step size is $\epsilon$, and the fraction of trajectories accepted is "acc.". Our definition of the step size is such that there is one evaluation of the fermion force per step, so a complete cycle of the Omelyan integration algorithm includes two fermion-action steps and six gauge-action steps. The physical lattice spacing given in this table uses the three flavor determination of $r_1 = 0.3117(6)(^{+12}_{-31})$ fm made using $f_\pi$ to set the scale on the asqtad ensembles [15]. It should be noted that when chiral and continuum limits of 2+1+1 flavor calculations are completed, a 2+1+1 flavor determination of $r_1$ will supercede this.

| $\frac{10}{g^2}$ | $am_l$ | $am_s$ | $am_c$ | $\epsilon_N$ | size | $u_0$ | $N_{lats}$ | $S_t$ | $L_t$ | $\epsilon$ | acc. | $r_1/a$ | $a$ (fm) |
|---|---|---|---|---|---|---|---|---|---|---|---|---|---|
| 5.8 | 0.013 | 0.065 | 0.838 | −0.3582 | $16^3 \times 48$ | 0.85535 | 1021 | 5 | 1.0 | 0.033 | 0.73 | 2.041(10) | $0.1527(^{+7}_{-16})$ |
| 6.0 | 0.0102 | 0.0509 | 0.635 | −0.2308 | $24^3 \times 64$ | 0.86372 | 1040 | 5 | 1.0 | 0.036 | 0.66 | 2.574(5) | $0.1211(^{+6}_{-12})$ |
| 6.3 | 0.0074 | 0.037 | 0.440 | −0.1205 | $32^3 \times 96$ | 0.874164 | 878 | 6 | 1.5 | 0.031 | 0.68 | 3.520(7) | $0.0886(^{+4}_{-9})$ |

fourth root of the corresponding determinant [13]. The final pseudofermion field implements the dynamical charm quark.

Rational function approximations were used for the fractional powers of the matrices [9, 14]. In the molecular dynamics evolution we used a 9'th order approximation for the pseudofermion field containing the light quarks, and a 7'th order approximation for the three regulator fields and the charm quark pseudofermion. For the heat bath updating of the pseudofermion fields and for computing the action at the beginning and end of the molecular dynamics trajectory we used 11'th order and 9'th order approximations. These approximations comfortably exceeded the required accuracy, but since a multimass conjugate gradient routine is used for the sparse matrix solutions, adding extra terms in these approximations has minimal cost.

In order to make this paper self-contained, we summarize the action in Appendix A, and discuss some algorithmic issues specific to the HISQ action in Appendices B, C, and D.
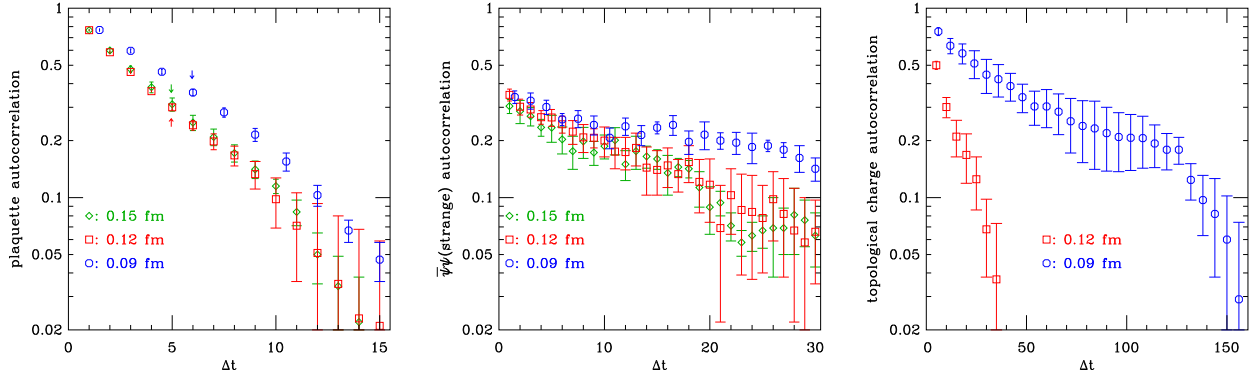
FIG. 1: Autocorrelation $C_{\Delta t}$ in simulation time of the plaquette (left panel), strange quark $\bar{\psi}\psi$ (center panel) and topological charge (right panel). Note that the horizontal scale is different in each of the three panels. Errors on the autocorrelation were estimated by dividing the time series into five subsets and averaging the autocorrelations from each subset. The vertical arrows in the left panel indicate the time separation between stored lattices, used in computing the potential, spectrum and other quantities.

## III. AUTOCORRELATIONS IN SIMULATION TIME

Estimating statistical errors on any physical quantity requires taking into account the fact that successive sample configurations are not completely statistically independent, and calculations of statistical errors that ignore these autocorrelations are generally underestimates of the true errors. The amount of autocorrelation depends strongly on the quantity under consideration, so we present autocorrelations for a few simple but relevant quantities. To parameterize autocorrelations we use the dimensionless coefficient

$$C_{\Delta t} = \frac{\langle x_i x_{i+\Delta t}\rangle - \langle x_i\rangle^2}{\langle x_i^2\rangle - \langle x_i\rangle^2} \tag{1}$$

where $x_i$ is the measurement at simulation time $i$ and $\Delta t$ is the time separation of the two measurements. As discussed above, in these simulations successive lattices were saved at time separations $\Delta t = 5$ for the $a = 0.15$ and $0.12$ fm ensembles, and $\Delta t = 6$ for the $0.09$ fm ensemble. However, measurements of the plaquette and $\bar{\psi}\psi$ were made every trajectory. Note that determination of these autocorrelation coefficients is numerically difficult, even on time series of order 1000 lattices. This is partly because of the practical necessity of using the average ($\langle x_i\rangle$) from our simulation, rather than the true average. (Note, however, that for the topological charge we know that the true average is zero.) Estimation of errors on these coefficients is also noisy. Here we have estimated the errors from the variance of autocorrelations measured on five separate segments of the time series, but for the central

6

TABLE II: Autocorrelation $C_{\Delta t}$ of various quantities between successive lattices in the ensembles. Lattices are separated by five time units for $a = 0.15$ and $0.12$ fm, and by six time units for $a = 0.09$ fm. As discussed in the text, the autocorrelations for $\bar{\psi}\psi$ are between estimates made with one random source. Autocorrelations for the correlators $\langle \pi(0)\pi(D) \rangle$ and $\langle \rho(0)\rho(D) \rangle$ are given at a spatial distance $D$ which is the minimum distance used in a typical fit for the mass. For the pion correlator these distances are $D = 15$, 20 and 30 respectively, and for the $\rho$ correlator they are $D = 6$, 7 and 10 respectively. For the pion and rho mass and $f_\pi$ the autocorrelations are from single elimination jackknife samples.

| operator | 0.15 fm | 0.12 fm | 0.09 fm |
|---|---|---|---|
| $\square$ | 0.311(25) | 0.300(10) | 0.359(14) |
| $\bar{\psi}\psi_{\text{light}}$ | 0.135(24) | 0.151(27) | 0.192(34) |
| $\bar{\psi}\psi_{\text{strange}}$ | 0.234(38) | 0.265(27) | 0.259(19) |
| $\langle \pi(0)\pi(D) \rangle$ | 0.034(40) | 0.084(46) | 0.177(21) |
| $\langle \rho(0)\rho(D) \rangle$ | 0.055(24) | 0.074(24) | 0.061(18) |
| $m_\pi$ | 0.008(14) | 0.182(35) | 0.249(51) |
| $f_\pi$ | 0.123(21) | 0.150(23) | 0.184(45) |
| $m_\rho$ | 0.036(38) | 0.045(09) | 0.002(24) |
| $Q_{\text{topo}}$ | na | 0.500(25) | 0.754(36) |

value quote the result from the full time series.

The autocorrelations can be taken into account either by blocking the data (averaging over intervals of time) and then computing the average of the blocked values, or by multiplying the error estimate ignoring autocorrelations by the factor

$$\sqrt{1 + 2 \sum_t C_t} \quad , \tag{2}$$

with the sum suitably truncated. For complicated functions of observables a jackknife analysis can be used, and Eqs. (1) and (2) applied to the sequence of jackknife results.

We begin with the plaquette and strange quark $\bar{\psi}\psi$, simple observables which were measured at each trajectory. The first two panels of Figure 1 show the autocorrelation of these quantities as a function of separation in simulation time. Here $\bar{\psi}\psi$ is estimated using a single random source vector. Thus part of its variance comes from the random source, and part

from the variation of the lattice. For this reason, its autocorrelation does not approach one at small time. We show the strange quark $\bar{\psi}\psi$ because it generally shows larger autocorrelations than the light quark $\bar{\psi}\psi$. Also, relevant to future ensembles at other light quark masses, it will be useful to compare autocorrelations using $\bar{\psi}\psi$ at a fixed physical quark mass. These two simple quantities provide a good illustration of how autocorrelations differ among various quantities.

Table II shows these quantities at the time separation of the stored lattices, and a selection of autocorrelations of more physically relevant quantities. In particular, it contains autocorrelations of the pion and rho correlators ($\langle\pi(0)\pi(D)\rangle$ and $\langle\rho(0)\rho(D)\rangle$) at a distance $D$ equal to the minimum distance that might be used in a mass fit, and would be one of the important contributors to the mass. This table also contains autocorrelations of single elimination jackknife measurements of the pion mass, the pion decay constant (amplitude of a pion correlator), and the rho meson mass.

The topological charge is generally expected to have a long autocorrelation time. In fact, in the continuum limit tunnelings would be expected to be completely suppressed in a simulation algorithm where the configurations evolve continuously. Such a simulation would still give correct results in infinite volume, but would have power-law finite volume effects [16]. The right panel in Fig. 1 shows the autocorrelation of the topological charge in the $a = 0.12$ and $0.09$ fm ensembles. As expected, the autocorrelation time is larger for this quantity than for the others, and is much larger on the finer ensemble. The long autocorrelation time means that it will be important to check the size of finite volume effects; such runs are planned.

In the sections below, the static quark potential was computed using block sizes of 50 time units for $a = 0.15$ and $0.12$ fm, and 60 time units for $a = 0.09$ fm. For the pseudoscalar meson plot, block sizes of 20 and 24 time units were used. Autocorrelations for the rho and nucleon masses are small, and were neglected here.

## IV. THE STATIC QUARK POTENTIAL

Although it is not a physical observable, the potential between two infinitely heavy test quarks is well defined on the lattice and can be computed with high precision and comparatively little effort. Therefore it has become conventional in lattice simulations to use
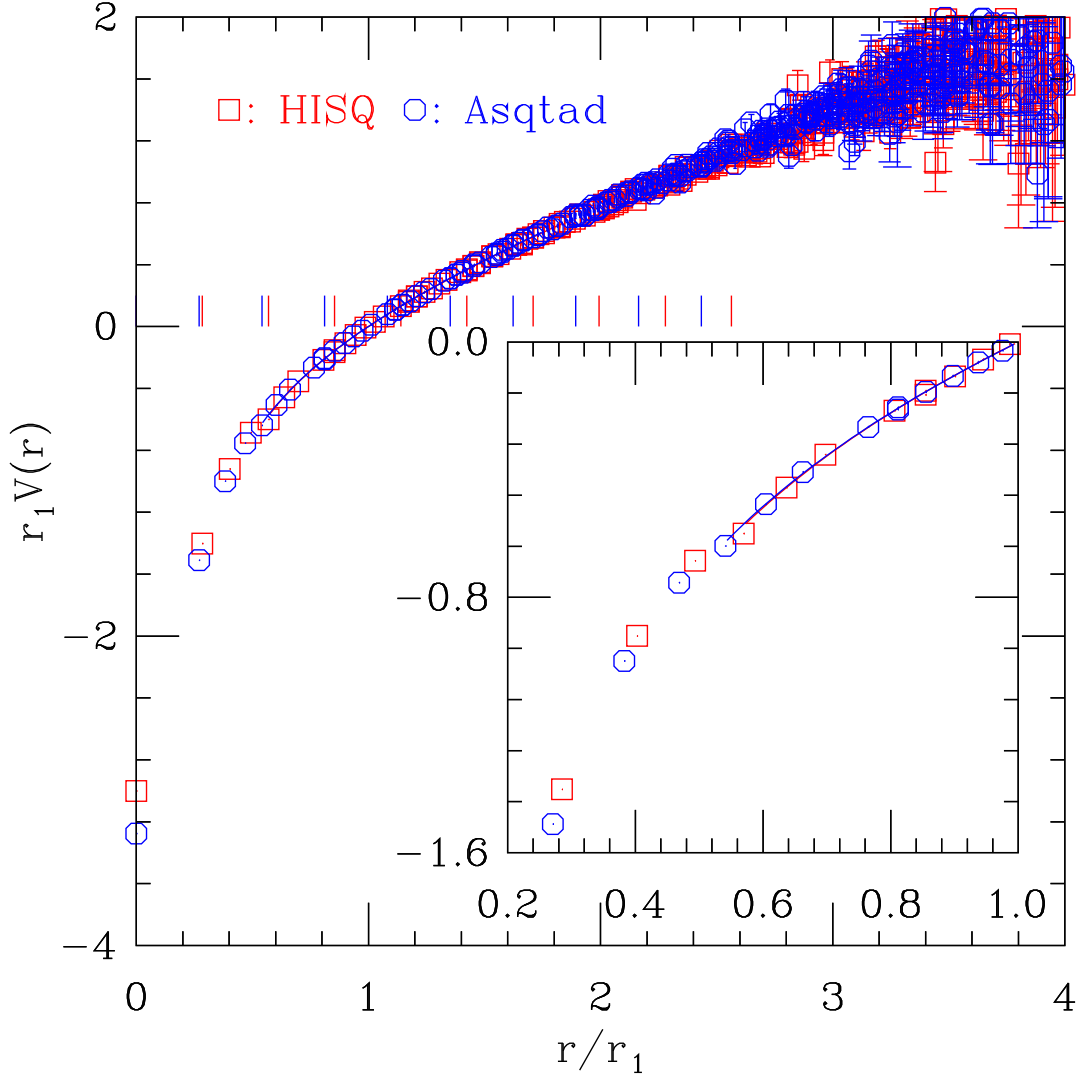
8

FIG. 2: The static quark potential with the HISQ and the asqtad actions. The HISQ results are from the $a \approx 0.09$ fm run, and the asqtad results are from a lattice with almost the same lattice spacing and light-quark mass about 0.2 times the correct strange quark mass ($am_l = 0.00465$). In order to match the potentials, the plot is in units of $r_1$, while rulers in units of the lattice spacing are shown at $r_1 V(r) = 0$. A constant has been added to each potential so that $V(r_1) = 0$. The solid lines (essentially superimposed) show the fit from Eq. (3) for the two runs, (evaluated with $\lambda$ set to zero). The inset magnifies a part of this plot at short distance to show the lattice artifacts discussed in the text.

a length scale based on the static quark potential to relate lattice simulations with different couplings, and to translate the dimensionless results of lattice simulations into physical units. We generally use $r_1$ defined by $r_1^2 F(r_1) = -1$, where $F(r)$ is the force $-\frac{\partial V(r)}{\partial r}$. The scale $r_0$ defined by $r_0^2 F(r_0) = -1.65$ is also commonly used. (The idea behind scales of this form [17] is that they locate the transition region between the Coulomb potential at short distances, $r^2 F(r) = -\frac{4}{3}\alpha$, and the linear potential at long distances, $r^2 F(r) = -\sigma r^2$.)

In order to determine $r_1$, we measure the static potential at discrete distances $r^2/a^2 = n_x^2 + n_y^2 + n_z^2$, and, for a range of $r$ approximately centered at $r_1$, we fit it to the functional form[18]

$$V(R) = C + \frac{B}{R} + \sigma R + \lambda \left( \frac{1}{R}\bigg|_{lat} - \frac{1}{R} \right) . \tag{3}$$

Here $\frac{1}{R}\big|_{lat}$ is the the lattice Coulomb potential, $\frac{1}{R}\big|_{lat} = 4\pi \int \frac{d^3 p}{(2\pi)^3} D_{00}^{(0)}(p) e^{ipR}$, with $D_{00}^{(0)}(p)$ the free lattice gluon propagator calculated with the Symanzik improved gauge action, and $1/R$ is the continuum Coulomb potential.

Figure 2 shows the static quark potential at $a \approx 0.09$ fm for the HISQ ensemble and a corresponding asqtad ensemble. Overall, the two potentials are very similar. For reference, the value of $r_1/a$ for this HISQ ensemble in Table I came from a fit to the range $\sqrt{5} \le r/a \le 6$, or $0.63 < r/r_1 < 1.70$. The inset in Fig. 2 makes visible some of the lattice artifacts at short distance. In particular, the HISQ point at $r/r_1 = 0.57$ and the asqtad point at $0.53$ correspond to separation $(2,0,0)$ along a lattice axis, and are visibly displaced below the trend. Note that artifacts of this kind are not decreased with the HISQ action, and we do not expect them to be decreased. In fact, in the continuum limit we expect them to be described by Eq. (3) with $\lambda = B$. (The fit to this potential has $B = -0.441(6)$ and $\lambda = -0.52(11)$.) Artifacts like this, at fixed number of lattice spacings, simply move to $r = 0$ in the continuum limit. Also note that these artifacts diminish quickly with increasing $r$. For example, the HISQ point at $r/r_1 = 0.95$ is really two points, with $\vec{r}/a = (3,0,0)$ and $(2,2,1)$, and the difference between the two potential values is invisible. We expect that these short distance lattice artifacts in the static quark potential are mostly controlled by the gauge actions, which differ only in the fermion contributions to the one loop corrections.

We do expect scaling violations proportional to $a^4$ and to $a^2 \alpha^2$ at physical distances for both actions, and these would be visible in quantities like $r_0/r_1$ or $r_1\sqrt{\sigma}$. However, it is not possible to make a definitive comparison of scaling violations in these quantities between the

TABLE III: Parameters of the potential fits in Fig. 2. As discussed in the text, in this comparison the fit ranges for the HISQ potential were chosen to match those used for the asqtad potential, and so these tabulated parameters differ slightly from those used in the rest of this paper. Note that the lattice mass is regularization dependent — in both of these ensembles the light quark mass is about one fifth of the correct strange quark mass.

|  | asqtad | HISQ |
| --- | --- | --- |
| Fit range | 2.01–6.5 | 2.01–6.5 |
| Time separations | 5–6 | 5–6 |
| $10/g^2$ | 7.085 | 6.30 |
| $am_l/am_s/am_c$ | 0.00465/0.031/na | 0.0074/0.037/0.440 |
| $Ca$ | 0.849(3) | 0.824(3) |
| $B$ | −0.432(4) | −0.450(5) |
| $\sigma r_1^2$ | 0.568(6) | 0.554(6) |
| $r_1/a$ | 3.697(7) | 3.510(7) |

two actions yet, since the addition of the dynamical charm quark to the HISQ simulations could also have small effects on these quantities.

For reference, Table III shows the parameters of the fits in Fig. 2, defined in Eq. (3). Note that in this figure the fitting range used for the HISQ run is the same as used for the asqtad ensemble, and so differs from that used in finding the value of $r_1/a$ in Table I. Also note that the quantity $\sigma r_1^2$ parameterizes the potential in the range around $r_1$, and should not be used as a measurement of the long distance string tension. Finally, note that since the dimensionful parameters are expressed in units of $r_1$, which is found from the same fit, one relation between $B$ and $\sigma$ is automatically enforced. In Fig. 2 this constraint forces both fits to have the same slope at $r = r_1$ (since $r_1$ is defined by the slope (force) at this distance), and a constant was subtracted to make both fits be zero at this point.

## V. SCALING TESTS

Reduction of taste splittings among the pion masses with HISQ valence quarks was demonstrated with quenched gauge fields in Refs. [1, 2], and with asqtad sea quarks in
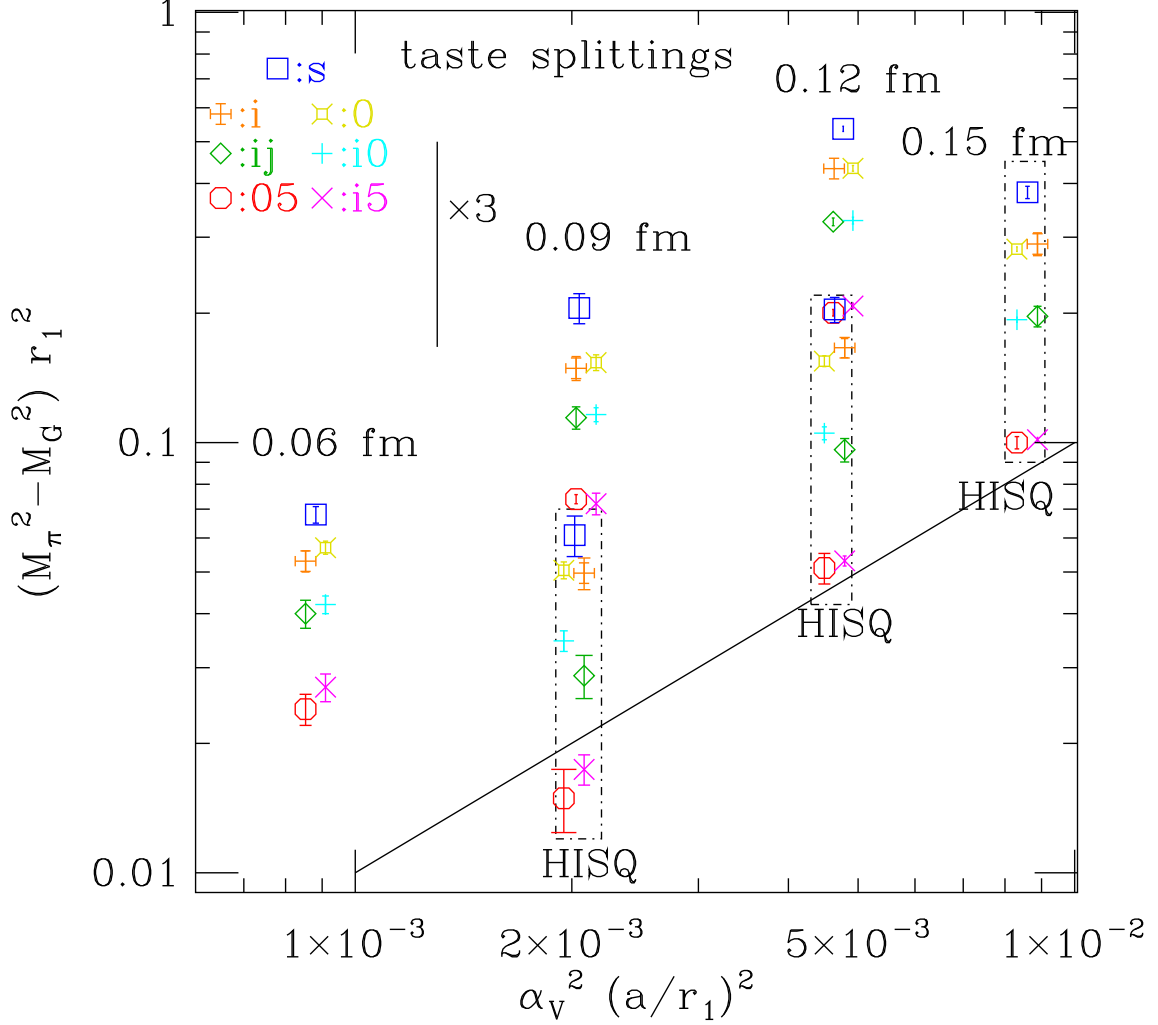
FIG. 3: Taste splittings among the pions. The asqtad results used configurations with 2+1 flavors of dynamical quarks, and the HISQ results 2+1+1 flavors. The quantity plotted is $r_1^2 \left( M_\pi^2 - M_G^2 \right)$, where $M_\pi$ is the mass of the non-Goldstone pion and $M_G$ is the mass of the Goldstone pion. Reading from top to bottom, the non-Goldstone pions are the $\pi_s$ (box), $\pi_0$ (fancy box), $\pi_i$ (fancy plus), $\pi_{io}$ (plus), $\pi_{ij}$ (diamond), $\pi_{i5}$ (cross) and $\pi_{05}$ (octagon). $r_1^2 \left( M_\pi^2 - M_G^2 \right)$ is known to be almost independent of the light-quark mass. The vertical bar at the upper left shows the size of a factor of three, roughly the observed reduction in taste splittings, while the sloping solid line shows the theoretically expected dependence on lattice spacing. Nearly degenerate points have been shifted horizontally to improve their visibility.

12

Ref. [3], and there is little reason to expect it to be different with dynamical HISQ sea quarks. However, in view of the importance of this quantity, we show splittings for all of the different tastes of pions in Fig. 3, comparing results with HISQ quarks (both valence and sea) to earlier results with asqtad quarks. In this figure, we see that the expected reduction in taste splittings happens, with roughly a factor of three reduction relative to asqtad calculations at the same lattice spacing.

The main purpose of this study was to see if the improvements in the action designed to reduce taste symmetry violations translate into decreased lattice spacing dependence in other quantities. We begin with the mass of the light-quark vector meson, or $\rho$. In Fig. 4 we show the mass of the $\rho$ meson in units of $r_1$. Here we have asqtad results for several light-quark masses at each lattice spacing, but HISQ results for only one light-quark mass. The light-quark masses themselves are regularization dependent, so to plot asqtad and HISQ results on the same footing we use the Goldstone pion mass in units of $r_1$ for the horizontal axis. Note that for $m_l = 0.2m_s$, the light-quark mass used in the HISQ simulations, and for the lattice sizes used here ($\leq 2.9$ fm), the vector meson is stable against decay to two pions. Results for the nucleon mass are similar, and are shown in Fig. 5. In Figs. 4 and 5 the HISQ masses show smaller dependence on the lattice spacing than the asqtad masses, with the same continuum limits within the statistical errors. Roughly speaking, the HISQ results are similar to the asqtad results at the next smaller lattice spacing.

Although we have chosen to present these results as improved scaling of the $\rho$ and nucleon masses, since we are plotting the dimensionless quantities $M_\rho r_1$ and $M_N r_1$, they could equally well be described as improved scaling of $r_1$ when a hadron mass is chosen to be the length standard.

The pseudoscalar meson decay constants are important for lattice determinations of CKM matrix elements, and can be computed with high precision. In fact, our current best determination of $r_1$ in physical units comes from matching the asqtad lattice results to the physical value of $f_\pi$. These decay constants for light quarks have been extensively studied using the asqtad ensembles [4, 20]. The HPQCD collaboration has computed these decay constants in a mixed action calculation, with HISQ valence quarks on the asqtad sea quark ensembles, and used them in a determination of the physical value of $r_1$ [21]. Figure 6 shows the pseudoscalar decay constant with one of the valence quarks fixed at approximately the strange quark mass as a function of the mass of the other valence quark. (At the physical
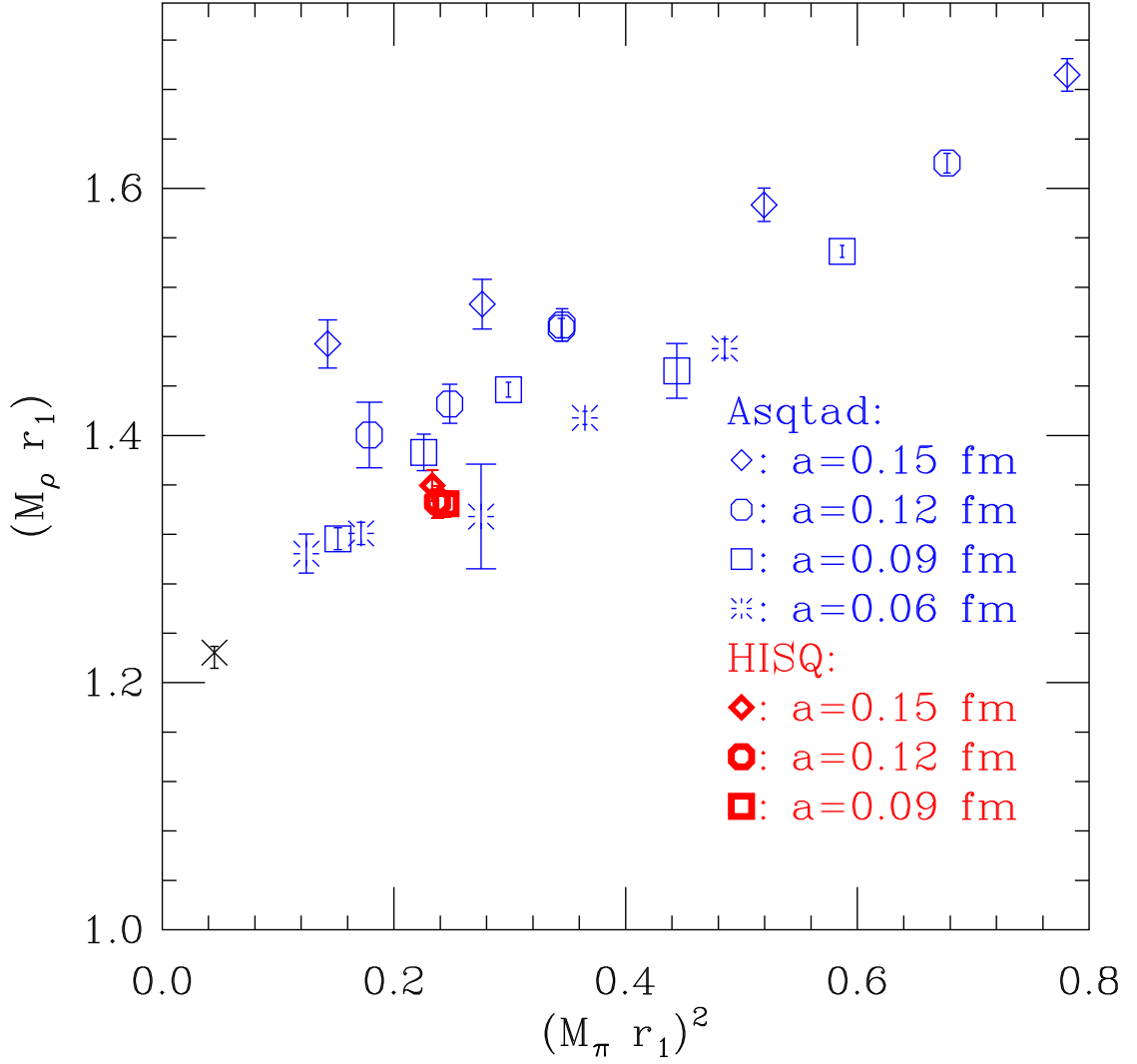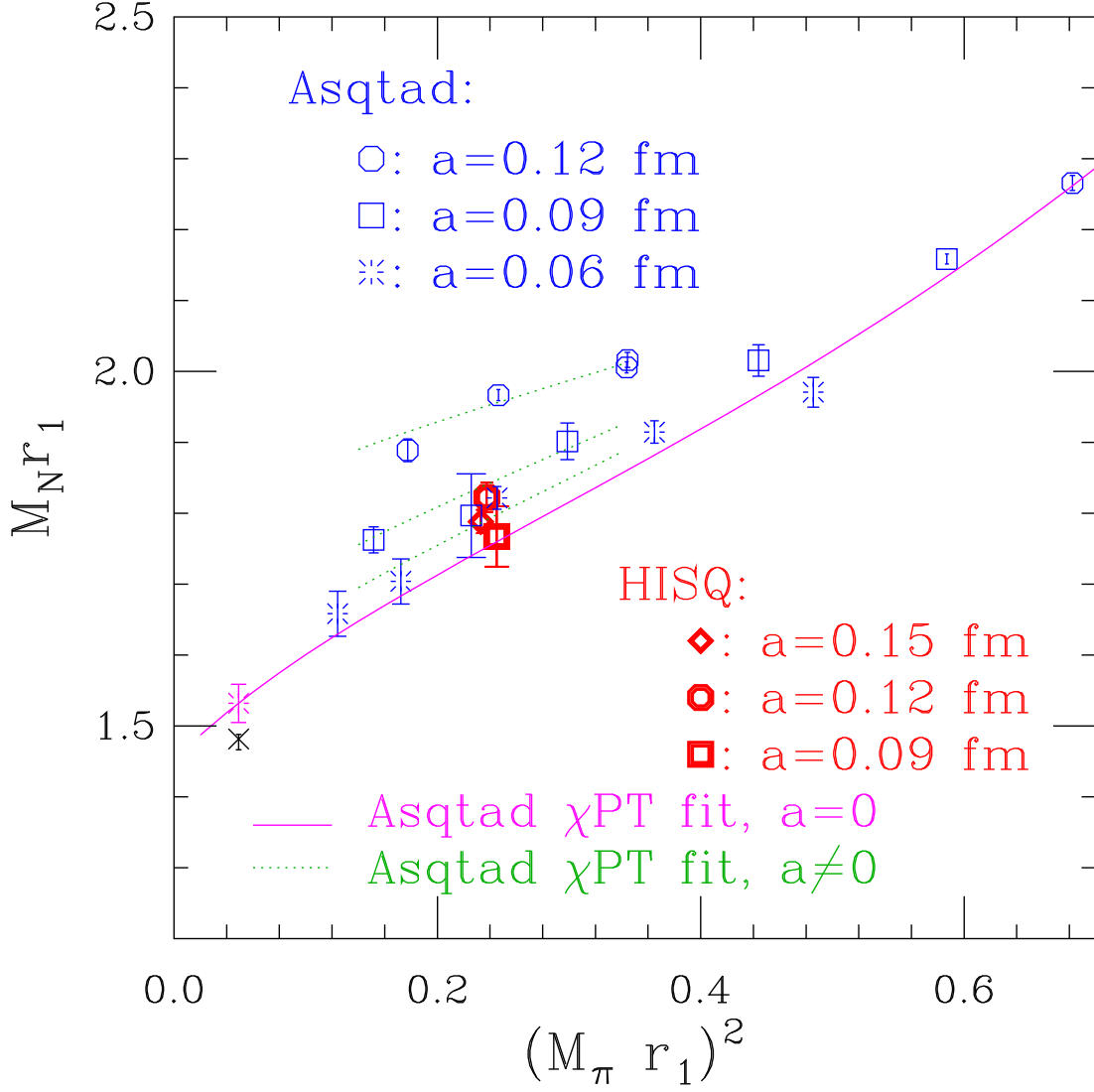
FIG. 4: Vector meson ($\rho$) masses in units of $r_1$. Here the bold (red) points are the HISQ simulations with $m_l = 0.2m_s$, and the lighter (blue) points are asqtad results for various light quark masses. The $a \approx 0.06$ fm asqtad point immediately to the right of the $a \approx 0.09$ fm HISQ point has been displaced to the right to make it visible. It in fact falls on top of the $a \approx 0.09$ fm HISQ point. The cross sign at lower left is the physical $\rho$ mass. The error on the physical mass point is just the error on the physical value of $r_1$.

FIG. 5: Nucleon masses in units of $r_1$. Here the bold (red) points are the HISQ simulations with $m_l = 0.2m_s$, and the lighter (blue) points are asqtad results for various light quark masses. The cross at lower left is the physical nucleon mass. The solid magenta line is a continuum extrapolation of a chiral perturbation theory fit to the asqtad nucleon masses, while the dotted green lines are from the same fit at finite lattice spacing [19].

light-quark mass, this is just $f_K$.) To facilitate the comparison, we have used the ratio of the light quark mass to the corrected strange quark mass in the corresponding ensemble for the horizontal axis. The reduction in lattice artifacts is obvious, and it can also be seen that the HISQ points lie near the continuum limit of the asqtad points. Once again, we remark
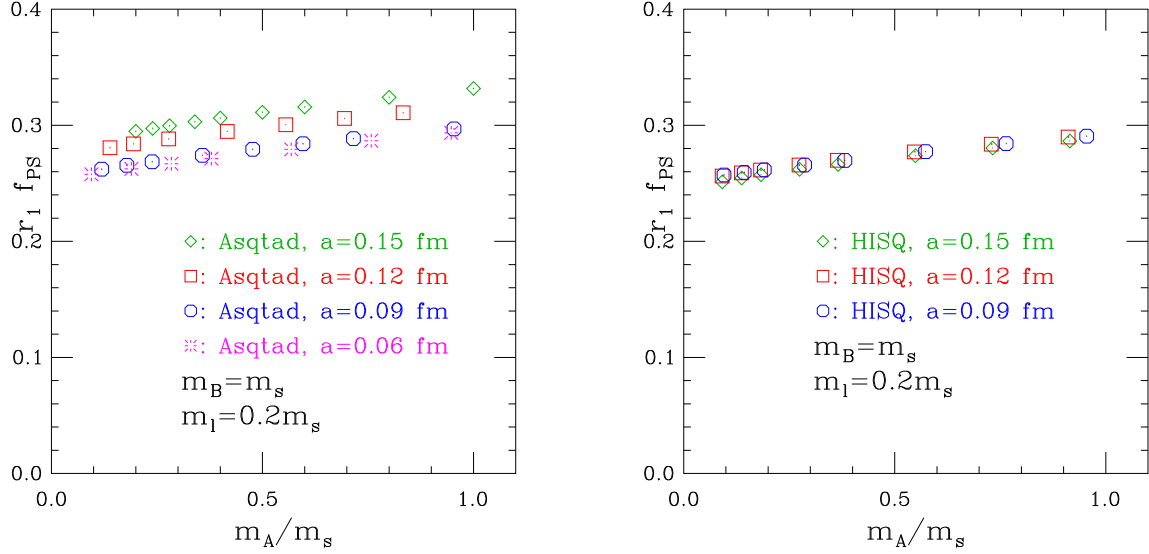
FIG. 6: Pseudoscalar decay constant. One valence-quark mass, $m_A$, is varied while the second is held fixed near the strange-quark mass. All ensembles used a light sea quark mass of about 0.2 times the strange-quark mass. The left hand panel shows asqtad results for four different lattice spacings and the right hand panel shows HISQ results for three lattice spacings.

that since the plotted quantity is $r_1 f_{PS}$, this could equally well be described as scaling of $r_1$ or scaling of $f_{PS}$.

The topological susceptibility is a particularly important test here, since it is computed solely from the gluon configurations that are generated, without involving HISQ or asqtad valence quarks. Therefore improvements in the scaling of the topological susceptibility directly test whether the change of the sea-quark action has the expected effect on the gluon configurations that are generated. Our technique for calculating the topological susceptibility is set out in detail in Ref. [23]. Here we just note that this technique is based on measurement of a density-density correlator, and hence is not limited by long autocorrelation times for the overall topological charge. Figure 7 shows the topological susceptibility for most of the asqtad ensembles, and HISQ results for the $a \approx 0.12$ fm and $a \approx 0.09$ fm ensembles. The HISQ point with $a \approx 0.12$ fm lies near the asqtad points with $a \approx 0.09$ fm, and the HISQ point with $a \approx 0.09$ fm is near the asqtad points with $a \approx 0.06$ fm, demonstrating a decrease in lattice artifacts. Note that the HISQ points are to the left of the corresponding asqtad points, which are indicated by arrows in the figure. This is because the horizontal axis is the mass of the taste singlet pion (the heaviest pion taste), and the reduction in taste symmetry breaking moves the points to the left. It is the movement down relative to the asqtad points that represents an improvement in the gluon configurations.

TABLE IV: Lattice spacings in fm from $r_1 = 0.3117$ fm, $f_{ss}$ with asqtad valence quarks, and $f_{ss}$ with HISQ valence quarks. The first five columns identify the ensemble by the sea-quark action, the gauge coupling $10/g^2$, and the sea-quark masses. The horizontal line separates ensembles with asqtad sea quarks (above) from those with HISQ sea quarks (below). The values for HISQ valence quarks on asqtad sea ensembles are taken from Ref. [21]. The errors on $a(r_1)$ are statistical only — they do not include the errors in $r_1 = 0.3117(6)(^{+12}_{-31})$ fm. Similarly, the errors on $a(f_{ss} - \text{asqtad})$ and $a(f_{ss} - \text{HISQ})$ for the HISQ ensembles do not include any errors in the physical value of $f_{ss}$. The numbers following the $f_{ss}$ lattice spacings are the value of the valence strange quark mass $am_s$ at which the desired ratio is obtained. We use the values $f_{ss} = 181.5$ MeV and $f_{ss}/M_{ss} = 0.2647$ from Ref. [21].

| Action | $10/g^2$ | $am_l$ | $am_s$ | $am_c$ | $a(r_1)$ | $a(f_{ss} - \text{asqtad})$ | $am_s$ | $a(f_{ss} - \text{HISQ})$ | $am_s$ |
|--------|----------|--------|--------|--------|----------|-----------------------------|--------|----------------------------|--------|
| asqtad | 6.76 | 0.01 | 0.05 | – | 0.1178(2) | 0.1373(2) | 0.0467 | 0.1264(11) | 0.0553 |
| asqtad | 7.09 | 0.0062 | 0.031 | – | 0.0845(1) | 0.0905(3) | 0.0286 | 0.0878(7) | 0.0362 |
| asqtad | 7.46 | 0.0036 | 0.018 | – | 0.0588(2) | 0.0607(1) | 0.0187 | 0.0601(5) | 0.0233 |
| asqtad | 7.81 | 0.0028 | 0.014 | – | 0.0436(2) | 0.0444(1) | 0.0133 | 0.0443(4) | 0.0163 |
| HISQ | 5.80 | 0.013 | 0.065 | 0.838 | 0.1527(7) | na | na | 0.1558(3) | 0.0720 |
| HISQ | 6.00 | 0.0102 | 0.0509 | 0.635 | 0.1211(2) | na | na | 0.1244(2) | 0.0549 |
| HISQ | 6.30 | 0.0074 | 0.037 | 0.440 | 0.0884(2) | na | na | 0.0900(1) | 0.0374 |

## VI.   USING f$_{ss}$ TO SET THE SCALE

In Figs. 4–6 it can be seen that $r_1 f_K$ and the hadron masses in units of $r_1$ all increase as the lattice becomes coarser. This common dependence on lattice spacing could be absorbed into a lattice spacing dependence of $r_1$. Put more simply, we could use one of these quantities to set the lattice spacing. Such a procedure has been introduced and studied by the HPQCD collaboration in Ref. [21]. In particular, they use the decay constant of a fictitious "unmixed $\bar{s}s$" pseudoscalar meson, which is an isospin non-singlet meson with both valence quarks having mass $m_s$, to set the scale. We call this decay constant $f_{ss}$. Like $r_1$, $f_{ss}$ is not a quantity that can be directly determined from experiment, and so, like $r_1$, its physical value is eventually determined by matching to some precisely known quantity such as $f_\pi$ or mass splittings of heavy quark mesons. In practice, the HPQCD collaboration determines $f_{ss}$ and
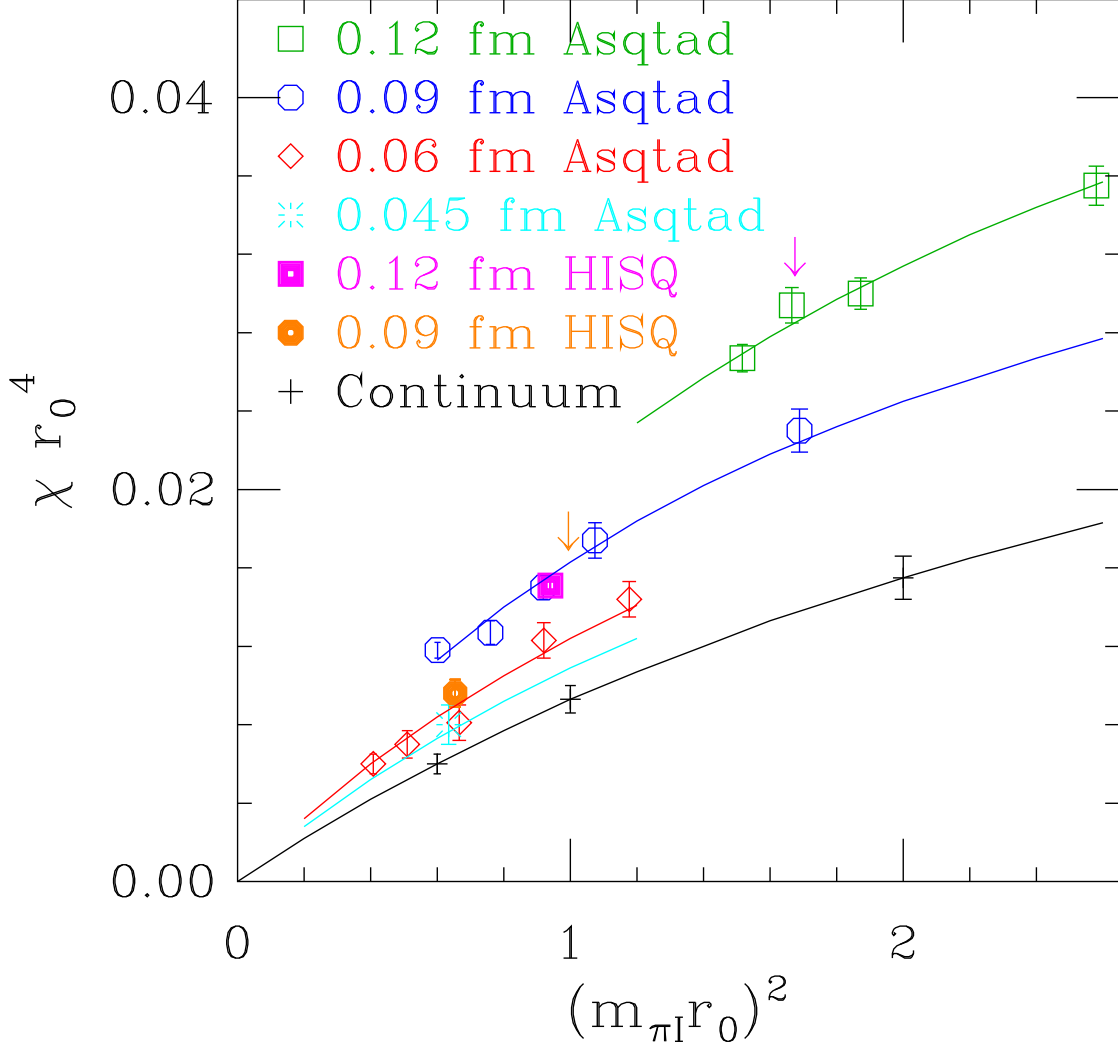
FIG. 7: The topological susceptibility. Points with the asqtad action are shown for several lattice spacings and quark masses, and the HISQ results for $a \approx 0.12$ fm and $a \approx 0.09$ fm with $m_l = 0.2 m_s$. For the horizontal axis we use the mass of the taste singlet pion, since in lowest order chiral perturbation theory the topological susceptibility is a function of this mass [22]. The curves in the figure come from a chiral perturbation theory fit to the asqtad data. The asqtad results are updated from Ref. [24] and are discussed further in Refs. [4, 23]. The two arrows indicate the locations of asqtad points with lattice spacing and quark mass similar to the two HISQ points. (In the case of the $a \approx 0.09$ fm HISQ point, the quark mass falls between two of the masses of the asqtad points.)

the corresponding meson mass $M_{ss}$ using a next-to-leading-order chiral fit (augmented with discretization corrections) to their lattice data, and inputs of the experimental values for $f_\pi$, $f_K$, $M_\pi$ and $M_K$. In fact, lowest order chiral perturbation theory and these experimental values alone (without lattice data) gets within $\sim 1\%$ of the HPQCD results [21]. We prefer not to input the experimental value $f_K$ in such determinations, since we take $f_K$ as an output of our lattice calculations that gives a result for $V_{us}$ [4, 20]. Indeed, $f_\pi$, $M_\pi$ and $M_K$ alone are adequate for determining the physical scale and the quark masses $m_l$ and $m_s$, and hence all light-quark quantities.

An advantage of using $f_{ss}$ to set the scale on a given lattice ensemble is that it can be determined to high accuracy in the simulations. However, it has the disadvantage that it depends on the choice of valence quarks, so the lattice spacing assigned to a particular ensemble will depend slightly on whether it is determined with asqtad quarks, HISQ quarks, or some other formalism.

Table IV shows the lattice spacings of the three HISQ ensembles used in this paper, and some comparable asqtad ensembles, using $r_1$ and $f_{ss}$ as the length standards. For the asqtad ensembles, we show the effect of using either asqtad or HISQ valence quarks to determine the lattice spacing. Note that, as expected, the differences among the scale determinations decrease as the lattice spacing decreases. The value of $f_{ss}$ and the corresponding strange quark mass $am_s$ were determined by fitting a quadratic polynomial through masses and decay constants at valence masses equal to 1.0, 0.8 and 0.6 times the sea strange quark mass. Table IV also shows the value of the strange quark mass $am_s$ given by this interpolation or extrapolation. Figure 8 shows the differences in length scale (relative to the determination from $r_1$) as a function of lattice spacing. In this figure it can be seen that these differences are vanishing in the expected way as the lattice spacing decreases.

In Fig. 9 we show the rho mass data from Fig. 4 replotted using $f_{ss}$ to set the scale. Replotting the nucleon masses in Fig. 5 would produce similar results. (Of course, one could then make a plot showing the dependence of $r_1 f_{ss}$ on sea-quark mass and lattice spacing.)


## VII. CONCLUSIONS

Using simulations with a fixed and unphysically large light-quark mass, we see that dimensionless ratios of several hadronic quantities show smaller dependence on lattice spacing
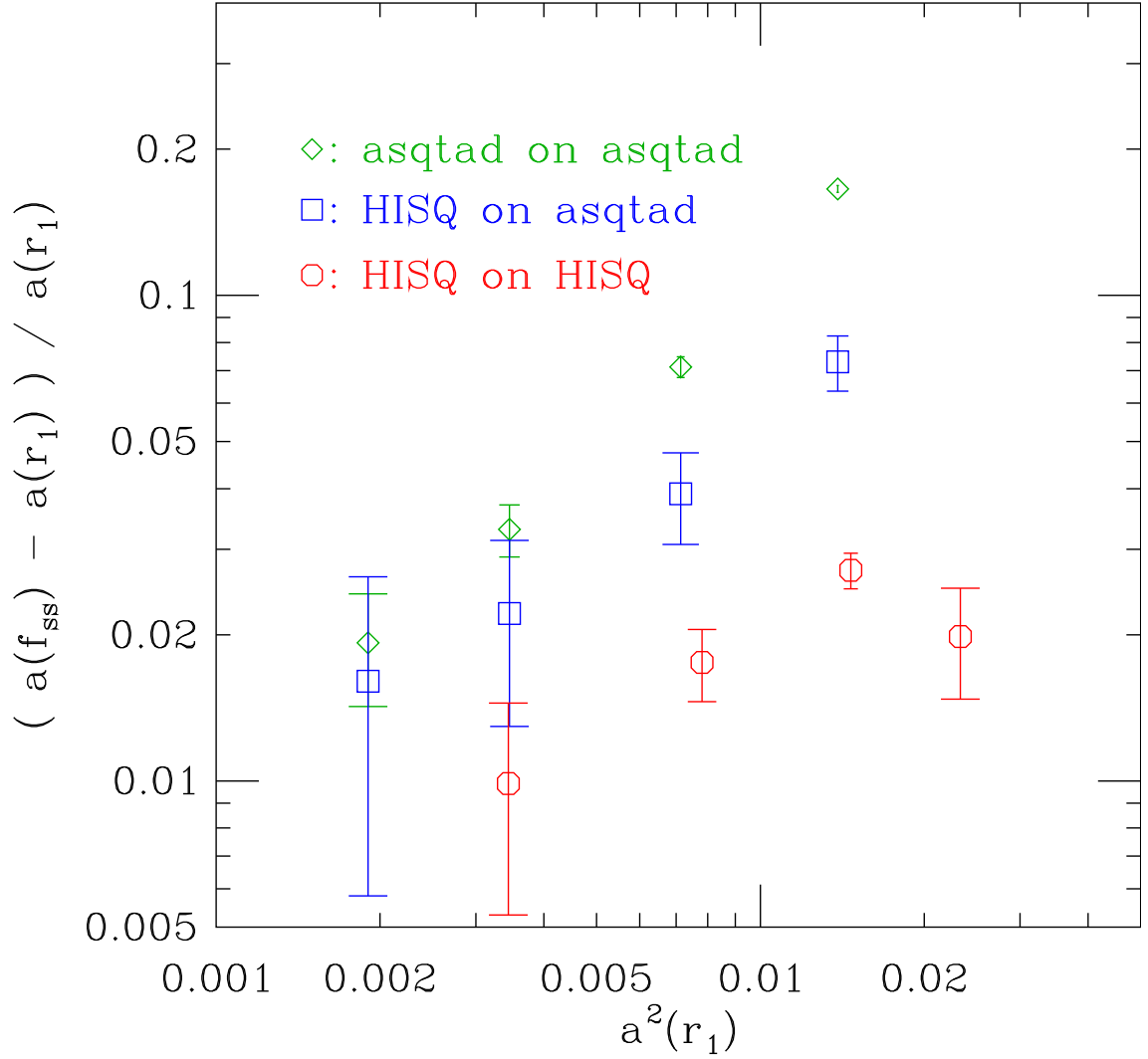
FIG. 8: Differences in determinations of the length scale using different standards. In the legend, the symbol types are labelled as "valence on sea". The "HISQ on asqtad" points are taken from Ref. [21].

with the HISQ action than with the asqtad action. Roughly, for the quantities that we checked, HISQ simulations at lattice spacing $a$ appear to have similar lattice artifacts as asqtad simulations at lattice spacing $\frac{2}{3}a$, leading to substantial savings in simulation costs. This program is continuing with computations at different light sea-quark masses, so that both the extrapolation to the continuum limit and the extrapolation to the physical light-quark mass can be controlled.
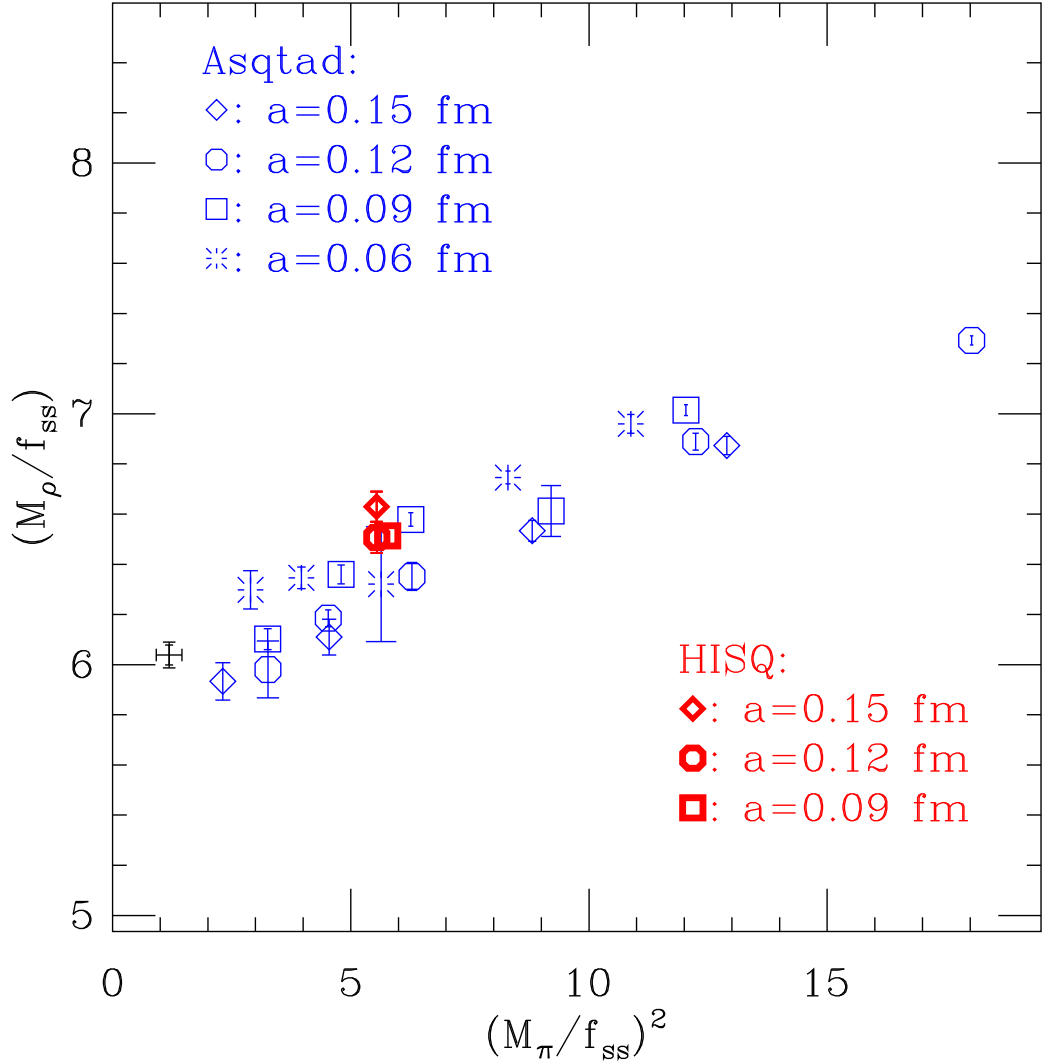
FIG. 9: Vector meson ($\rho$) masses in units of $f_{ss}$. The data and the meaning of the symbols are the same as in Fig. 4. The vertical and horizontal scales in the figure correspond to the same ranges as in Fig. 4.

**Acknowledgements**

**Appendix A: Gauge and fermion actions**

For completeness, we summarize the gauge and fermion actions in this appendix.

The gauge action is a tadpole-improved [25] one-loop-Symanzik-improved gauge action [26] including the effects of the quark loops in the one-loop coefficients [8]. The number of flavors $n_f$ is set to four in these simulations.

This gauge action involves three kinds of loops: the $1 \times 1$ loop, or plaquette $P$, the $2 \times 1$ loop, or rectangle $R$, and the twisted loop $T$, which traverses paths such as $+\hat{x}, +\hat{y}, +\hat{z}, -\hat{x}, -\hat{y}, -\hat{z}$. Then

$$S_g = \beta \left( C_P \sum_P \left( 1 - \frac{1}{3}\mathrm{Re}\,\mathrm{Tr}(P) \right) + C_R \sum_R \left( 1 - \frac{1}{3}\mathrm{Re}\,\mathrm{Tr}(R) \right) + C_T \sum_T \left( 1 - \frac{1}{3}\mathrm{Re}\,\mathrm{Tr}(T) \right) \right),$$

(A1)

where the sums run over all distinct positions and orientations of the loops. The coefficients are

$$
\begin{aligned}
C_P &= 1.0 \\
C_R &= \frac{-1}{20u_0^2} \left( 1 - (0.6264 - 1.1746 n_f) \ln(u_0) \right) \\
C_T &= \frac{1}{u_0^2} (0.0433 - 0.0156 n_f) \ln(u_0) \quad .
\end{aligned}
$$

(A2)

In this expression the strong coupling constant appears in the form $\alpha_s = -\ln(u_0)/1.303615$. With this normalization $\beta = \frac{10}{g^2}$. We determine the tadpole coefficient $u_0$ from the average plaquette, $u_0 = (\langle \mathrm{Re\,Tr}P\rangle /3)^{1/4}$.

The fermion factor in the partition function is

$$\ln(S_f) = \prod_f (\det(2\slashed{D} + 2m_f))^{1/4} \quad . \tag{A3}$$

The Dirac operator $\slashed{D}$ is constructed from smeared links. Two levels of smearing are used, with a projection onto an element of U(3) after the first smearing. The fundamental gauge links are $U_\mu(x)$, the fat links after a level one fat7 smearing are $V_\mu(x)$, the reunitarized links are $W_\mu(x)$, and the fat links after level two asqtad smearing are $X_\mu(x)$. The first level smeared links $V$ are constructed from the $U$ as a sum over products of links along paths from $x$ to $x + \hat{\mu}$, or parallel transports.

$$V_\mu(x) = \sum_{paths} \prod_{path} U^{(\dagger)}(path) \tag{A4}$$

Table V gives the coefficients used in the two levels of smearing. The nearest neighbor part of $\slashed{D}$ uses the twice-smeared links $X$ while the third nearest neighbor part uses the once-smeared and unitarized links $W$:

$$
\begin{aligned}
2\slashed{D}_{x,y} = \sum_{\mu} \quad & \left\{\delta_{x+\hat{\mu},y}X_\mu(x) - \delta_{x-\hat{\mu},y}X_\mu^\dagger(x-\hat{\mu})\right\} \\
+(1+\epsilon_N) \quad & \left\{\delta_{x+3\hat{\mu},y}W_\mu(x)W_\mu(x+\hat{\mu})W_\mu(x+2\hat{\mu})\right. \\
& \left. - \delta_{x-3\hat{\mu},y}W_\mu^\dagger(x-3\hat{\mu})W_\mu^\dagger(x-2\hat{\mu})W_\mu^\dagger(x-\hat{\mu})\right\} \quad .
\end{aligned}
\tag{A5}
$$

In Eq. (A5) and Table V, $\epsilon_N$ is a mass-dependent correction to the tree-level improvement of the quark dispersion relation, or the "Naik term." This correction is negligible and set to zero for the light and strange quarks. For the charm quark we use

$$\epsilon_N = -\frac{27}{40}(am_c)^2 + \frac{327}{1120}(am_c)^4 - \frac{15607}{268800}(am_c)^6 - \frac{73697}{3942400}(am_c)^8 \ . \tag{A6}$$

In this expression $am_c$ is the bare mass in the quark action, and this formula combines Eqs. (24) and (26) in Ref. [3]. The numerical values of $\epsilon_N$ used in our simulations are given in Table I.

TABLE V: Paths and coefficients used in smearing the links. It is understood that all distinct rotations and reflections of each path are used in the action. In specifying paths in this table, directions $\hat{x}$ and $\hat{y}$, etc. are different. The multiplicity is the number of such paths contributing to a single smeared link. The first block of the table gives the coefficients used in the "fat7" smearing used to construct $V$ from $U$. The second block gives the coefficients in the "asqtad+" smearing used to compute $X$ from the unitarized links $W$, and the final line is the coefficient of the third nearest neighbor term. Note that the coefficient of the "Lepage" term that corrects the form factor at small momenta is twice that of the single smearing asqtad action.

| Name | Path | Multiplicity | Coefficient |
|---|---|---|---|
| Single link | $+\hat{x}$ | 1 | 1/8 |
| 3-staple | $+\hat{y} + \hat{x} - \hat{y}$ | 6 | 1/16 |
| 5-staple | $+\hat{y} + \hat{z} + \hat{x} - \hat{z} - \hat{y}$ | 24 | 1/64 |
| 7-staple | $+\hat{y} + \hat{z} + \hat{t} + \hat{x} - \hat{t} - \hat{z} - \hat{y}$ | 48 | 1/384 |
| Single link | $+\hat{x}$ | 1 | $1/8 + 3/4 + 1/8(1 + \epsilon_N)$ |
| 3-staple | $+\hat{y} + \hat{x} - \hat{y}$ | 6 | 1/16 |
| 5-staple | $+\hat{y} + \hat{z} + \hat{x} - \hat{z} - \hat{y}$ | 24 | 1/64 |
| 7-staple | $+\hat{y} + \hat{z} + \hat{t} + \hat{x} - \hat{t} - \hat{z} - \hat{y}$ | 48 | 1/384 |
| "Lepage" | $+\hat{y} + \hat{y} + \hat{x} - \hat{y} - \hat{y}$ | 6 | $-1/8$ |
| "Naik" | $+\hat{x} + \hat{x} + \hat{x}$ | 1 | $-1/24(1 + \epsilon_N)$ |

## Appendix B: HISQ force calculation details

Here we summarize the details of the HISQ force calculation. For clarity in this and the next appendices we suppress the $x$-dependence and the direction index in the notation of the links. Most of this material appeared earlier in Ref. [10]. For the force calculation we adopted the strategy of Refs. [27] and [28] , in which the derivative of the smeared action is calculated by repetitive application of the chain rule:

$$\frac{\partial S_f}{\partial U} = \frac{\partial S_f}{\partial X} \frac{\partial X}{\partial W} \frac{\partial W}{\partial V} \frac{\partial V}{\partial U} \ , \tag{B1}$$

where $S_f$ is the fermion part of the action, $U$ are fundamental gauge links, $V$, the fat links after level one fat7 smearing, $W$, the reunitarized links, and $X$, the fat links after level two asqtad smearing. In our code, for the parts that involve smearing, we follow the same
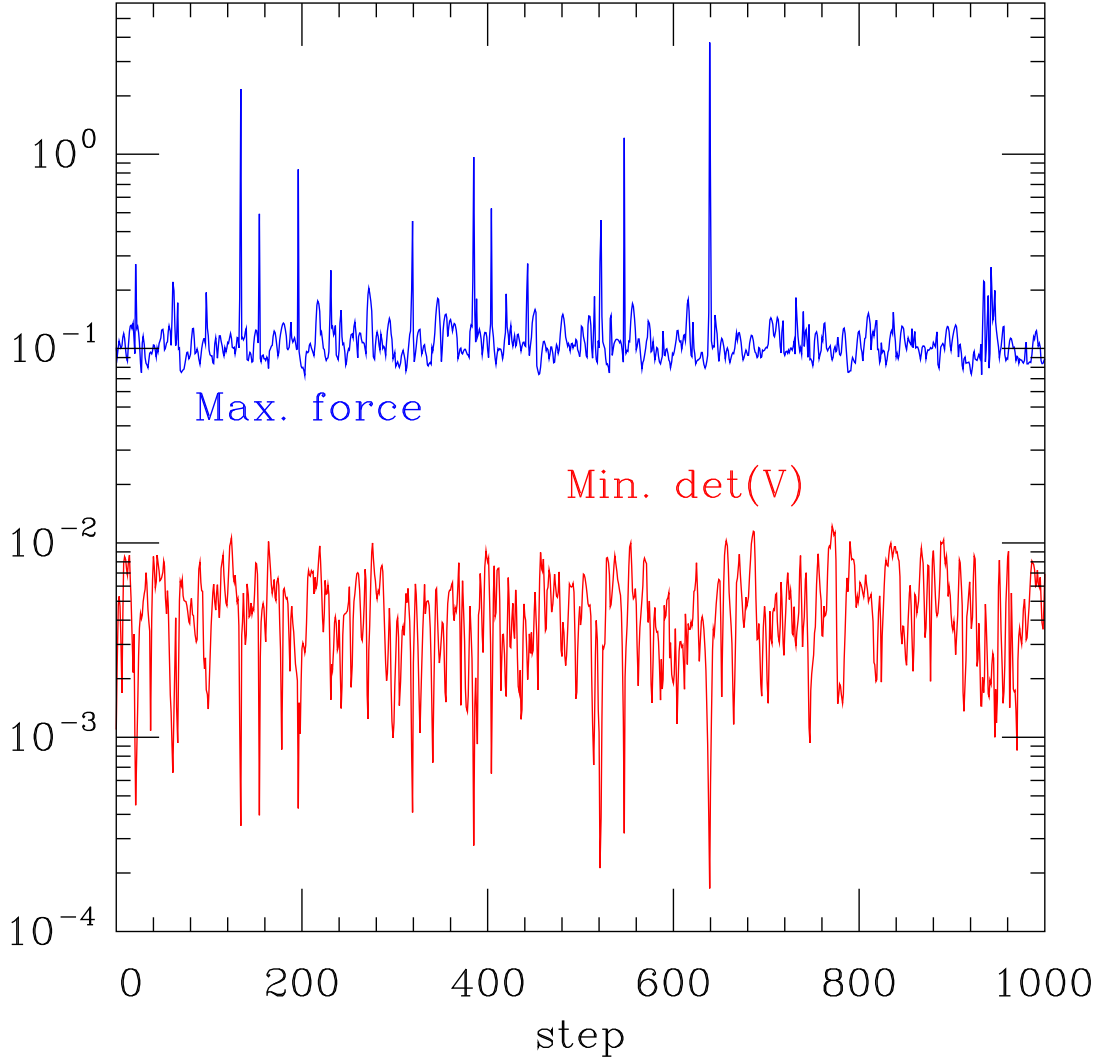
FIG. 10: Time history of the maximum (over lattice sites) magnitude of the fermion force and the minimum determinant of the fattened links after the first level of smearing ($V$). This exploratory run was done on a $20^3 \times 64$ lattice at $\beta = 6.75$, $am_l = 0.2am_s$, $am_s = 0.05$, $am_c = 0.6$ and $u_0 = 0.9$. This approximately corresponds to the $a \approx 0.12$ fm ensemble in Table I at $\beta = 6.0$. The difference in $\beta$ is due to the use of a different gauge action in the earlier studies.

procedure as for the asqtad action. This procedure is described in Refs. [29] and [30], so we do not repeat it here. The algorithm for the reunitarization part is detailed below.

We have chosen to project links to U(3), rather than SU(3) as in the original HPQCD/UKQCD formulation, for two reasons:

1. SU(3) projection requires calculation of the third root of the determinant, which involves a phase that can initially be restricted to, *e.g.*, the interval $[-\pi/3, \pi/3)$. However, during the molecular dynamics evolution, this phase has to evolve continuously (to prevent the appearance of $\delta$ function-like forces) and may cross into $[\pi/3, 2\pi/3)$ interval, and so on. Thus, SU(3) projection requires tracking the evolution of the phase for each link during molecular dynamics.

2. For the U(3) group, different methods of projection yield the same answer for the projected link, $W$.

For instance, the default method in our code is polar projection: one builds a Hermitian matrix

$$Q = V^\dagger V \tag{B2}$$

and then

$$W = VQ^{-1/2} \tag{B3}$$

belongs to U(3), *i.e.*,

$$W^\dagger W = \left(Q^{-1/2}\right)^\dagger V^\dagger V Q^{-1/2} = Q^{-1/2}QQ^{-1/2} = 1. \tag{B4}$$

It is important that closed form expressions for $Q^{-1/2}$ can be derived [31] and, thus, the whole procedure can be implemented analytically.

One may expect, given that $Q^{-1/2}$ is a singular operation, that when one of the eigenvalues of $Q$ is close to 0, the numerical accuracy in evaluation of $W$ becomes poor. In fact, in simulations one occasionally encounters large deviations from unitarity:

$$\left|W^\dagger W - 1\right| \sim O(1). \tag{B5}$$

Such situations are rare, but the contribution of (systematic) errors of this kind can be large. Therefore, we also implemented the singular value decomposition (SVD) algorithm, which is slower, but is used only in exceptional cases. We decompose:

$$V = A\Sigma B^\dagger, \tag{B6}$$

$A, B \in$ U(3) and $\Sigma$ is a positive, diagonal matrix. (The values on the diagonal are called the singular values of $V$.) Then we have, simply,

$$W = AB^\dagger. \tag{B7}$$

It is easy to see that (B3) gives the same result as (B7):

$$Q = V^\dagger V = B\Sigma A^\dagger A \Sigma B^\dagger = B\Sigma\Sigma B^\dagger = B\Sigma B^\dagger B\Sigma B^\dagger = \left(B\Sigma B^\dagger\right)^2 ,$$

$$Q^{-1/2} = \left(B\Sigma B^\dagger\right)^{-1} = \left(B^\dagger\right)^{-1}\Sigma^{-1}B^{-1} = B\Sigma^{-1}B^\dagger ,$$

$$W = A\Sigma B^\dagger B\Sigma^{-1}B^\dagger = AB^\dagger ,$$

as it should be. The SVD algorithm of Golub and Reinsch [32] is numerically stable even in the case of exactly zero eigenvalues.

Another popular projection algorithm is "trace maximization" [33]: find $W \in \mathrm{U}(3)$ such that it maximizes

$$\Omega = \mathrm{ReTr}\left\{V^\dagger W\right\} . \tag{B8}$$

Let us again use SVD on $V$:

$$V = A\Sigma B^\dagger \quad \Rightarrow \quad \Omega = \mathrm{ReTr}\left\{B\Sigma A^\dagger W\right\} = \mathrm{ReTr}\left\{\Sigma A^\dagger W B\right\} . \tag{B9}$$

Since $\Sigma$ is positive, clearly $\Omega$ is maximized when

$$A^\dagger W B = 1 \quad \Rightarrow \quad W = AB^\dagger \tag{B10}$$

and we arrive at (B7) again. In the SU(3) case an extra phase present in (B9) would lead to $W$ different from (B7). To summarize, we use the polar projection (B3) replaced by SVD if small eigenvalues of $Q$ are encountered.

Appendix C gives the details of calculation of $Q^{-1/2}$ and its derivative $\partial Q^{-1/2}/\partial V$ within the approach of Refs. [34] and [31] based on the Cayley-Hamilton theorem.

Let us now turn to the calculation of the force. During the molecular dynamics evolution, one encounters (more often on coarser ensembles) matrices $V$ that have small eigenvalues. Let us consider the U(1) group for simplicity. Then $V$ is just an arbitrary complex number $V = re^{i\theta}$. The projection onto U(1) is $W = e^{i\theta}$. The derivative that enters the force calculation is

$$\frac{\partial W}{\partial V} \equiv \left(\frac{\partial W}{\partial V}\right)_{V^\dagger} = \frac{\partial(W, V^\dagger)}{\partial(V, V^\dagger)} = \frac{\partial(W, V^\dagger)}{\partial(r, \theta)} \frac{\partial(r, \theta)}{\partial(V, V^\dagger)} = \frac{1}{2r}, \tag{B11}$$

Thus the derivative is inversely proportional to the magnitude of $V$, or, in the U(3) case, to the smallest singular value of $V$ (or eigenvalue of $Q$), which is not protected from being zero. Thus, on rare occasions one has to deal with exceptionally large forces that give large

contributions to the action, but originate from a single link. In Fig. 10 we show the evolution of the minimal $\det |V|$ over the lattice and maximal value of the norm of the fermion force on a logarithmic scale. One can easily see the correlation: the lower $\det |V|$, the higher the force.

To circumvent this problem we introduce a "cutoff" in the force calculation by replacing:

$$W = VQ^{-1/2} \quad \rightarrow \quad W = V(Q + \delta I)^{-1/2}, \tag{B12}$$

where $I$ is the unit matrix, whenever the smallest eigenvalue of $Q$ is less than $\delta$. In the ensembles used in this paper we set $\delta = 5 \times 10^{-5}$. In tuning $\delta$, we weigh two competing issues: The value of $\delta$ should be large enough to suppress an exceptional contribution from a link, but small enough not to modify too many forces on the lattice. If $\delta$ is too large, the evolution will be smooth, but the fluctuation of the action will be large, usually leading to rejection of the trajectory. Note that we modify $W$ only in the force calculation, and we use the original Eq. (B3), or Eq. (B7) for nearly singular matrices, to calculate the action at the accept/reject step. That is, the modification (B12) amounts to using a different guiding Hamiltonian during the evolution, while the Metropolis step insures the desired distribution.

### Appendix C: Algebra for reunitarized links and their derivatives

To make this presentation self-contained we include Eqs. (C1)-(C11) from Hasenfratz, Hoffmann and Schaefer [31], preserving the notation of the original.

The inverse square root of a non-singular matrix $Q$ entering Eq. (B3) is given by the Cayley-Hamilton theorem as a polynomial of $Q$:

$$Q^{-1/2} = f_0 + f_1 Q + f_2 Q^2. \tag{C1}$$

Since $Q$ is Hermitian, it has nonnegative eigenvalues that can be found by solving the characteristic equation

$$g^3 - c_0 g^2 - \left(c_1 - \frac{1}{2}c_0^2\right)g - \left(c_2 - c_0 c_1 + \frac{1}{6}c_0^3\right) = 0, \tag{C2}$$

where

$$c_n = \frac{1}{n+1}\operatorname{tr} Q^{n+1}, \quad n = 0, 1, 2. \tag{C3}$$

The solution of the cubic equation (C2) is

$$g_n = \frac{c_0}{3} + 2\sqrt{S}\,\cos\left(\frac{\theta}{3} + (n-1)\frac{2\pi}{3}\right)\,, \quad n = 0, 1, 2, \qquad \text{(C4)}$$

where

$$S = \frac{c_1}{3} - \frac{c_0^2}{18}\,, \quad R = \frac{c_2}{2} - \frac{c_0 c_1}{3} + \frac{c_0^3}{27}\,, \quad \theta = \arccos\left(\frac{R}{S^{3/2}}\right)\,. \qquad \text{(C5)}$$

It is convenient to define the symmetric polynomials of the square roots of the eigenvalues

$$
\begin{aligned}
u &= \sqrt{g_0} + \sqrt{g_1} + \sqrt{g_2}\,, \\
v &= \sqrt{g_0 g_1} + \sqrt{g_0 g_2} + \sqrt{g_1 g_2}\,, \\
w &= \sqrt{g_0 g_1 g_2}\,.
\end{aligned}
\qquad \text{(C6)}
$$

In the diagonalized form the expression (C1) can be rewritten as an equation for $f_i$

$$
\begin{pmatrix}
1 & g_0 & g_0^2 \\
1 & g_1 & g_1^2 \\
1 & g_2 & g_2^2
\end{pmatrix}
\begin{pmatrix}
f_0 \\
f_1 \\
f_2
\end{pmatrix}
=
\begin{pmatrix}
g_0^{-1/2} \\
g_1^{-1/2} \\
g_2^{-1/2}
\end{pmatrix}
\qquad \text{(C7)}
$$

which has the solution

$$
\begin{aligned}
f_0 &= \frac{-w(u^2 + v) + uv^2}{w(uv - w)}\,, \\
f_1 &= \frac{-w - u^3 + 2uv}{w(uv - w)}\,, \\
f_2 &= \frac{u}{w(uv - w)}\,.
\end{aligned}
\qquad \text{(C8)}
$$

The derivative $\partial f_i / \partial c_j$ can be written as

$$B_{ij} \equiv \frac{\partial f_i}{\partial c_j} = \sum_{k=0}^{2} \frac{\partial f_i}{\partial g_k}\frac{\partial g_k}{\partial c_j}\,. \qquad \text{(C9)}$$

After rescaling (C9) by the common denominator

$$C_{ij} \equiv d B_{ij}\,, \quad d = 2w^3(uv - w)^3 \qquad \text{(C10)}$$

a closed-form expression for the symmetric matrix $C_{ij}$ has been derived in Ref. [31]

$$
\begin{aligned}
C_{00} &= -w^3u^6 + 3vw^3u^4 + 3v^4wu^4 - v^6u^3 - 4w^4u^3 - 12v^3w^2u^3 \\
&\quad + 16v^2w^3u^2 + 3v^5wu^2 - 8vw^4u - 3v^4w^2u + w^5 + v^3w^3 \,, \\
C_{01} &= -w^2u^7 - v^2wu^6 + v^4u^5 + 6vw^2u^5 - 5w^3u^4 - v^3wu^4 - 2v^5u^3 \\
&\quad - 6v^2w^2u^3 + 10vw^3u^2 + 6v^4wu^2 - 3w^4u - 6v^3w^2u + 2v^2w^3 \,, \\
C_{02} &= w^2u^5 + v^2wu^4 - v^4u^3 - 4vw^2u^3 + 4w^3u^2 + 3v^3wu^2 - 3v^2w^2u + vw^3 \,, \\
C_{11} &= -wu^8 - v^2u^7 + 7vwu^6 + 4v^3u^5 - 5w^2u^5 - 16v^2wu^4 - 4v^4u^3 + 16vw^2u^3 \\
&\quad - 3w^3u^2 + 12v^3wu^2 - 12v^2w^2u + 3vw^3 \,, \\
C_{12} &= wu^6 + v^2u^5 - 5vwu^4 - 2v^3u^3 + 4w^2u^3 + 6v^2wu^2 - 6vw^2u + w^3 \,, \\
C_{22} &= -wu^4 - v^2u^3 + 3vwu^2 - 3w^2u \,. \tag{C11}
\end{aligned}
$$

In the following, differentiation with respect to $V$ at fixed $V^\dagger$ is always assumed. We use explicit color indices to show how different contractions and direct products of matrices are built.

The derivatives that enter in the calculation of the fermion force are

$$
\frac{\partial W_{ij}}{\partial V_{kl}} = \frac{\partial (V_{im}(Q^{-1/2})_{mj})}{\partial V_{kl}} = \delta_{ik}(Q^{-1/2})_{lj} + V_{im}\frac{\partial(Q^{-1/2})_{mj}}{\partial V_{kl}}\,, \tag{C12}
$$

$$
\frac{\partial W_{ij}^\dagger}{\partial V_{kl}} = \frac{\partial ((Q^{-1/2})_{im}V_{mj}^\dagger)}{\partial V_{kl}} = \frac{\partial(Q^{-1/2})_{im}}{\partial V_{kl}}V_{mj}^\dagger \,. \tag{C13}
$$

Also,

$$
\frac{\partial Q_{ij}}{\partial V_{kl}} = V_{ik}^\dagger \delta_{lj}. \tag{C14}
$$

The central component of the calculation is

$$
\begin{aligned}
\frac{\partial(Q^{-1/2})_{ij}}{\partial Q_{pq}} &= \frac{\partial}{\partial Q_{pq}}\left(f_0\delta_{ij} + f_1Q_{ij} + f_2(Q^2)_{ij}\right) \\
&= \frac{\partial f_0}{\partial Q_{pq}}\delta_{ij} + \frac{\partial f_1}{\partial Q_{pq}}Q_{ij} + f_1\delta_{ip}\delta_{qj} + \frac{\partial f_2}{\partial Q_{pq}}(Q^2)_{ij} + f_2\left(\delta_{ip}Q_{qj} + Q_{ip}\delta_{qj}\right) \tag{C15}
\end{aligned}
$$

From the definition (C3) it follows that $\partial c_n/\partial Q_{pq} = (Q^n)_{pq}$. Then

$$
\frac{\partial f_k}{\partial Q_{pq}} = \sum_{n=0}^{2} \frac{\partial f_k}{\partial c_n}\frac{\partial c_n}{\partial Q_{pq}} = \sum_{n=0}^{2} B_{kn}(Q^n)_{pq} \,. \tag{C16}
$$

We define

$$P_{qp} \equiv \frac{\partial f_0}{\partial Q_{pq}} = B_{00}\delta_{qp} + B_{01}Q_{qp} + B_{02}(Q^2)_{qp}, \tag{C17}$$

$$R_{qp} \equiv \frac{\partial f_1}{\partial Q_{pq}} = B_{10}\delta_{qp} + B_{11}Q_{qp} + B_{12}(Q^2)_{qp}, \tag{C18}$$

$$S_{qp} \equiv \frac{\partial f_2}{\partial Q_{pq}} = B_{20}\delta_{qp} + B_{21}Q_{qp} + B_{22}(Q^2)_{qp}. \tag{C19}$$

Substituting (C17), (C18) and (C19) into (C15) and Eq. (C15) in (C12) and (C13) we obtain the final result

$$
\begin{aligned}
\frac{\partial W_{ij}}{\partial V_{kl}} &= \delta_{ik}(Q^{-1/2})_{lj} + \left[f_1(VV^\dagger)_{ik} + f_2(VQV^\dagger)_{ik}\right]\delta_{lj} + f_2(VV^\dagger)_{ik}Q_{lj} \\
&\quad + V_{ij}(PV^\dagger)_{lk} + (VQ)_{ij}(RV^\dagger)_{lk} + (VQ^2)_{ij}(SV^\dagger)_{lk}, \tag{C20}
\end{aligned}
$$

$$
\begin{aligned}
\frac{\partial W_{ij}^\dagger}{\partial V_{kl}} &= \left[f_1 V_{ik}^\dagger + f_2(QV^\dagger)_{ik}\right]V_{lj}^\dagger + f_2 V_{ik}^\dagger(QV^\dagger)_{lj} \\
&\quad + V_{ij}^\dagger(PV^\dagger)_{lk} + (QV^\dagger)_{ij}(RV^\dagger)_{lk} + (Q^2V^\dagger)_{ij}(SV^\dagger)_{lk}. \tag{C21}
\end{aligned}
$$

The calculation of the fermion force from the reunitarized links proceeds as follows:

1. The eigenvalues of the Hermitian matrix $Q$ are calculated with Eq. (C4).

2. det $|Q|$ is compared with the product $g_0 g_1 g_2$. If the relative error is larger than $10^{-8}$ or any eigenvalue is smaller than $10^{-8}$ the singular value decomposition of $V$ is performed and the eigenvalues are set to

$$g_i = \sigma_i^2, \quad i = 0, 1, 2, \tag{C22}$$

   where $\sigma_i$ are the diagonal elements of the matrix $\Sigma$ in Eq. (B6).

3. Additionally, if any of the eigenvalues is smaller than (an adjustable parameter) $\delta = 5 \times 10^{-5}$ the eigenvalues are modified to

$$g_i \rightarrow g_i + \delta. \tag{C23}$$

   (This corresponds to the force "cutoff" in Eq. (B12).)

4. With these eigenvalues the coefficients $f_i$ and the elements $B_{ij}$ are calculated from Eq. (C8) and (C11).

5. Finally, the force is calculated from Eq. (C20) and (C21).

In the MILC code we have also implemented two other methods for calculating $Q^{-1/2}$ and its derivative:

1. a rational function approximation,

2. an iterative evaluation of $Q^{-1/2}$ with the derivative replaced by finite difference.

We found that the analytic evaluation via Eq. (C20) and (C21) is superior to the other methods due to its higher precision and speed.

### Appendix D: Treatment of the HISQ charm quark

The tree-level discretization errors are $O((ap_\mu)^4)$ and are negligible for light quarks. However, at the lattice spacings listed in Table I, the charm quark mass is in the range $am_c \sim 0.4 - 0.8$ and therefore the discretization errors are larger. The leading tree-level $O((am_c)^4)$ error can be removed by retuning the coefficient of the third-nearest-neighbor (Naik) term [3], using the expansion in Eq. (A6). As can be seen from Table I, at the finest lattice, $a \approx 0.09$ fm, it is quite small, $\epsilon_N = -0.120471$. The effect of the correction in Eq. (A6) has been studied in Ref. [3]. To check the quality of charm quark physics in our ensembles, we computed the speed of light for the $\eta_c$ meson by calculating its propagator at several non-zero momenta. The result is shown in Fig. 11, where

$$c^2(p) = \frac{E^2(p) - E^2(0)}{p^2} \tag{D1}$$

and the momenta are rescaled by the lattice size $L_s$

$$n^2 = p^2 \left(\frac{L_s}{2\pi}\right)^2. \tag{D2}$$

For the finest $a \approx 0.09$ fm ensemble the error in the dispersion relation is below 2%. As expected, these $\eta_c$ dispersion relations are very similar to those found for HISQ valence quarks on asqtad sea quarks, shown in Table V of Ref. [3].

For dynamical simulations, the mass-dependent correction to the Naik term requires the use of different sets of smeared links for light quarks and the charm quark. Since the difference in the Naik term enters at the second level of smearing, it is advantageous to regroup the force calculation as described in the following. Let $X^{(0)}$ denote the fat links after level two asqtad smearing for the light quarks, for which $\epsilon_N$ is set to zero, and $X^{(c)}$
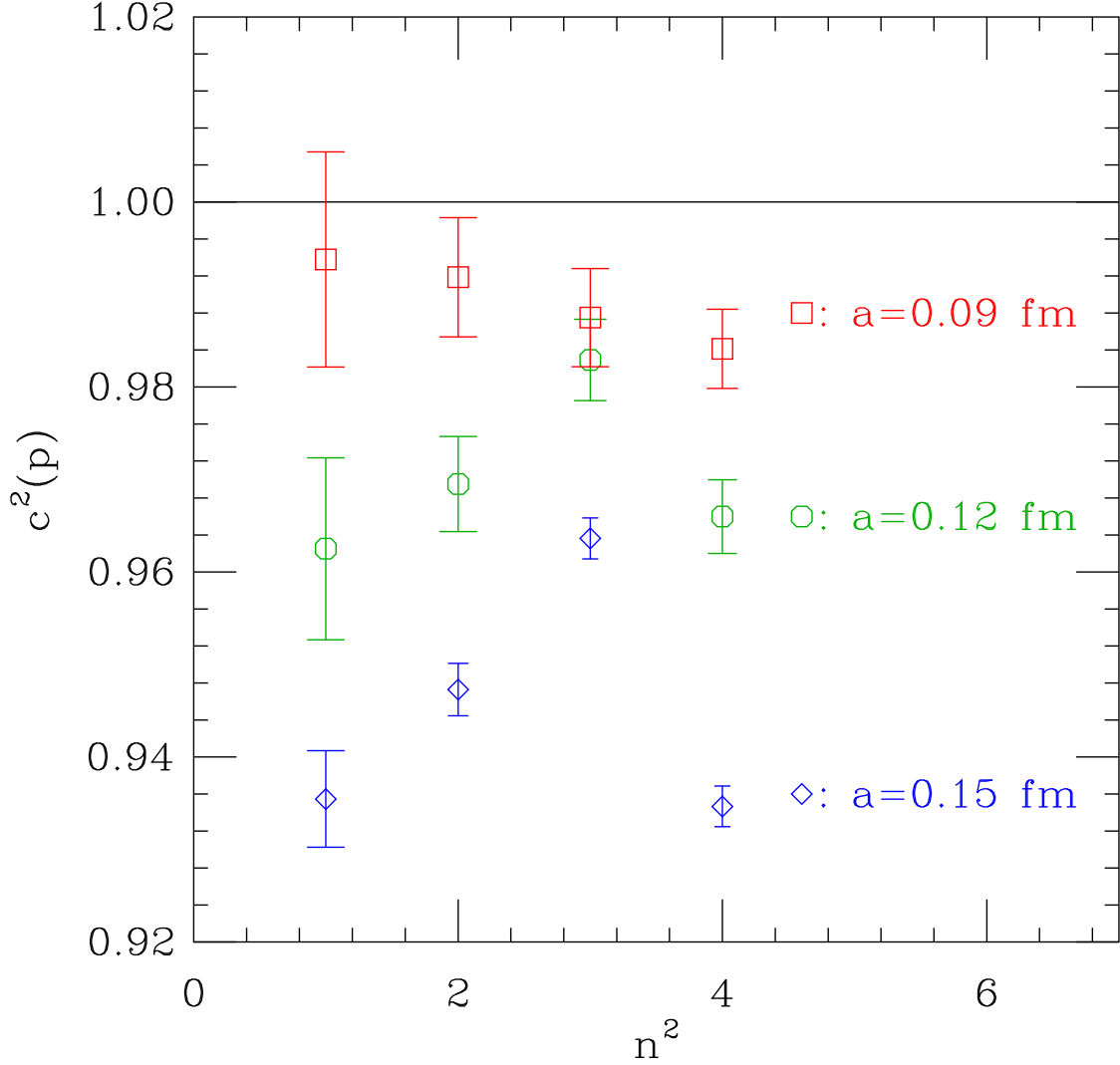
FIG. 11: The speed of light for the $\eta_c$ meson calculated at several values of momenta.

denote the fat links for the charm quark. Then the fat links for the charm quark can be written as

$$X^{(c)} = X^{(0)} + \epsilon_N \Delta X \,, \tag{D3}$$

where $\Delta X$ contains only one-link and three-link paths. (This can be easily seen from Table V.) The derivative is

$$\frac{\partial X^{(c)}}{\partial W} = \frac{\partial X^{(0)}}{\partial W} + \epsilon_N \frac{\partial \Delta X}{\partial W}. \tag{D4}$$

The fermion force in Eq. (B1) contains contributions from the light ($u$, $d$ and $s$) quarks, and

from the charm quark.

$$\frac{\partial S_f}{\partial U} = \frac{\partial S_f}{\partial X^{(0)}} \frac{\partial X^{(0)}}{\partial W} \frac{\partial W}{\partial V} \frac{\partial V}{\partial U} + \frac{\partial S_f}{\partial X^{(c)}} \frac{\partial X^{(c)}}{\partial W} \frac{\partial W}{\partial V} \frac{\partial V}{\partial U} \ . \tag{D5}$$

The calculation of the force for multiply smeared actions proceeds from the last level of smearing to the first one. Therefore, operations with $X^{(0)}$ and $X^{(c)}$ links are done first and can be combined before the reunitarization part:

$$\begin{aligned}
\frac{\partial S_f}{\partial U} &= \left( \frac{\partial S_f}{\partial X^{(0)}} \frac{\partial X^{(0)}}{\partial W} + \frac{\partial S_f}{\partial X^{(c)}} \frac{\partial X^{(c)}}{\partial W} \right) \frac{\partial W}{\partial V} \frac{\partial V}{\partial U} \\
&= \left( \left( \frac{\partial S_f}{\partial X^{(0)}} + \frac{\partial S_f}{\partial X^{(c)}} \right) \frac{\partial X^{(0)}}{\partial W} + \epsilon_N \frac{\partial S_f}{\partial X^{(c)}} \frac{\partial \Delta X}{\partial W} \right) \frac{\partial W}{\partial V} \frac{\partial V}{\partial U} \ . \tag{D6}
\end{aligned}$$

After the $\partial \Delta X / \partial W$ contribution is separated, the number of operations needed for the HISQ fermion force is reduced to slightly more than twice the number needed for the asqtad fermion force. This is because the most time-consuming part of the calculation is related to 3-, 5- and 7-staple paths that have high multiplicity. In our final form (D6) they are present only in $\partial X^{(0)} / \partial W$ and $\partial V / \partial U$.

---

[1] E. Follana *et al.*, Nucl. Phys. B (Proc. Suppl.) **129** and **130**, 447 (2004), [arXiv:hep-lat/0311004].

[2] E. Follana *et al.*, Nucl. Phys. B. (Proc. Suppl.) **129** and **130**, 384, 2004. [arXiv:hep-lat/0406021].

[3] E. Follana *et al.* [HPQCD Collaboration and UKQCD Collaboration], Phys. Rev. D **75**, 054502 (2007) [arXiv:hep-lat/0610092].

[4] A. Bazavov *et al.*, Rev. Mod. Phys. **82**, 1349 (2010),' [arXiv:0903.3598].

[5] C. T. H. Davies *et al.*, PoS LAT2006 082, (2006), [arXiv:hep-lat/0610110].

[6] E. Follana, C. T. H. Davies, G. P. Lepage, J. Shigemitsu, Phys. Rev. Lett. **100**, 062002 (2008), arXiv:0706.1726v2.

[7] C. T. H. Davies *et al.*, PoS LAT2008, 118 (2008), [arXiv:0810.3548].

[8] Zh. Hao *et al.* Phys. Rev. **D76**, 034507 (2007), [arXiv:0705.4660]; A. Hart, G. von Hippel and R.R. Horgan, Phys. Rev. D **79**, 074008 (2009), [arXiv:0812.0503].

[9] M.A. Clark and A.D. Kennedy, Nucl. Phys. Proc. Suppl. **129**, 850 (2004), [arXiv:hep-lat/0309084]; M. A. Clark and A. D. Kennedy, Phys. Rev. D **75**, 011502 (2007) [arXiv:hep-

lat/0610047]. M. A. Clark and A. D. Kennedy, Phys. Rev. Lett. **98**, 051601 (2007) [arXiv:hep-lat/0608015].

[10] A. Bazavov *et al.* [MILC Collaboration], PoS LATTICE2008, 033 (2008) [arXiv:0903.0874]; A. Bazavov *et al.*, PoS LAT2009 123 (2009), [arXiv:0911.0869].

[11] J.C. Sexton and D.H. Weingarten, Nucl. Phys. **B380**, 665 (1992).

[12] I.P. Omelyan, I.M. Mryglod, and R. Folk, Phys. Rev. **E65**, 056706 (2002); T. Takaishi and Ph. de Forcrand, Phys. Rev. **E73**, 036706 (2006), [arXiv hep-lat/0505020].

[13] M. Hasenbusch, Phys. Lett. **B519**, 177 (2001), [arXiv hep-lat/0107019]; M. Hasenbusch and K. Jansen, Nucl. Phys. **B659**, 299 (2003), [arXiv hep-lat/0211042].

[14] The rational function approximations were computed by a code derived from one written by Mike Clark. M.A. Clark, private communication.

[15] A. Bazavov *et al.*, PoS(LAT2009) 079 (2009), [arXiv:0910.3618]

[16] H. Leutwyler and A. V. Smilga, Phys. Rev. D **46**, 5607 (1992).

[17] R. Sommer, Nucl. Phys. **B411**, 839 (1994), [arXiv:hep-lat/9310022].

[18] UKQCD Collaboration, S.P. Booth *et al.*, Phys. Lett. **B294**, 385 (1992), [arXiv:hep-lat/9209008].

[19] C. Bernard *et al.*, PoS (LATTICE 2007) 137 (2007), [arXiv:0711.0021].

[20] C. Aubin *et al.* (MILC Collaboration), Phys. Rev. **D70**, 114501 (2004), [arXiv:hep-lat/0407028]; C. Bernard *et al.* (MILC Collaboration), PoS LAT2005, 025 (2006), [arXiv:hep-lat/0509137]; C. Bernard *et al.* (MILC Collaboration), PoS LAT2006, 163 (2006), [arXiv:hep-lat/0609053]; C. Bernard *et al.* (MILC Collaboration), PoS LAT2007, 090 (2007), [arXiv:0710.1118]; A. Bazavov *et al.* (MILC Collaboration), to appear in Pos LAT2009 [arXiv:0911.0472]; A. Bazavov *et al.* (MILC Collaboration), PoS LAT2009, 279 (2009), [arXiv:0910.3618]; A. Bazavov *et al.* (MILC Collaboration), PoS CD09, 007, 2009, arXiv:0910.2966.

[21] C.T.H. Davies *et al.*, [arXiv:0910.1229].

[22] C. Aubin and C. Bernard, Phys. Rev. **D68**, 034014, 2003, [arXiv hep-lat/0304014]; B. Billeter, C.E. DeTar and J. Osborn, Phys. Rev. **D70**, 077502, 2004, [arXiv hep-lat/0406032].

[23] A. Bazavov *et al.*, Phys. Rev. **D81**, 114501 (2010) [arXiv:1003.5695].

[24] C. Bernard *et al.*, PoS LAT2007, 310 (2007), [arXiv 0710.3124].

[25] G.P. Lepage and P.B. Mackenzie, Phys. Rev. D **48**, 2250 (1993).

[26] K. Symanzik, In: Recent Developments in Gauge Theories, edited by G. 't Hooft et al. (Plenum Press, New York, 1980), p. 313, (1980); K. Symanzik, Nucl. Phys. **B226**, 187 (1983); M. Lüscher and P. Weisz, Phys. Lett. **B158**, 250 (1985); M. Lüscher and P. Weisz, Commun. Math. Phys. **97**, 59 (1985); M.G. Alford *et al.*, Phys. Lett. **B361**, 87 (1995).

[27] W. Kamleh, D. B. Leinweber and A. G. Williams, Phys. Rev. D **70**, 014502 (2004) [arXiv:hep-lat/0403019].

[28] K. Y. Wong and R. M. Woloshyn, PoS LAT2007, 047 (2007) [arXiv:0710.0737].

[29] K. Orginos and D. Toussaint, Phys. Rev. D **59**, 014501 (1999), [hep-lat/9805009].

[30] M.A. Clark, A.D. Kennedy and Z. Sroczynski, Nucl. Phys. B [Proc. Suppl.] **140**, 835 (2005), [hep-lat/0409133].

[31] A. Hasenfratz, R. Hoffmann and S. Schaefer, JHEP **0705**, 029 (2007) [arXiv:hep-lat/0702028].

[32] G.H. Golub and C. Reinsch, Numerische Mathematik 14, 403 (1970)

[33] G. S. Bali and K. Schilling, Phys. Rev. D **46**, 2636 (1992).

[34] C. Morningstar and M. J. Peardon, Phys. Rev. D **69**, 054501 (2004) [arXiv:hep-lat/0311018].